Acta Geophysica (2025) 73:1775–1799
https://doi.org/10.1007/s11600-024-01439-8

RESEARCH ARTICLE - HYDROLOGY AND HYDRAULICS

Estimating future changes in streamflow and suspended sediment load under CMIP6 multi-model ensemble projections: a case study of Bitlis Creek, Turkey

Emrah Yalcin[1]

Received: 16 April 2024 / Accepted: 27 August 2024 / Published online: 27 September 2024

Abstract
The Euphrates-Tigris River Basin, which spans Turkey, Syria, Iraq, and Iran, is one of the most vulnerable zones to climate change. This study quantifies the impacts of changing climate on streamflow and suspended sediment load rates in the most threatened highlands region of the Euphrates-Tigris Basin, with the case of Bitlis Creek. In this evaluation, the multi-model ensemble approach is utilized to produce precipitation and temperature projections by analyzing the simulation performances of 24 global circulation models (GCMs) from the coupled model intercomparison project phase 6 (CMIP6). The Soil and Water Assessment Tool (SWAT) is used to estimate future streamflow and suspended sediment load rates over 25-year periods under the medium- and high-forcing shared socio-economic pathway (SSP) scenarios of SSP2-4.5 and SSP5-8.5. The results illustrate that the mean annual streamflow and suspended sediment load rates are expected to decrease by up to 8.5 and 21.4% under the SSP2-4.5 scenario, and by up to 20.9 and 40.7% under the SSP5-8.5 scenario, respectively. The projected shift from snowy to rainy winters leads to significant increases in winter streamflow and suspended sediment load rates, anticipated to reach 39.1 and 73.5%, respectively, during the 2075–2099 period for the SSP5-8.5 scenario. In contrast, declines in spring streamflow and suspended sediment load rates are projected to reach 40.9 and 60.0%, respectively, during the same period under the SSP5-8.5 scenario. These results suggest that the riparian countries should incorporate adaptive measures into their water resources management plans to ensure a sustained water supply in the coming decades.

Keywords Suspended sediment · CMIP6 · Multi-model ensemble · SWAT · LOADEST · Euphrates-Tigris River Basin

Introduction

Mountains and highlands serve as lifelines in socio-hydrological systems, as most rivers originate from such elevations (Adam et al. 2009; Milano et al. 2015; Viviroli et al. 2003, 2007). Snow at high altitudes contributes significantly to downstream discharge and plays a substantial role in the hydrological cycle (Immerzeel et al. 2020; Viviroli et al. 2007). Due to the high sensitivity of snow accumulation and ablation to air temperature, the impact of global warming is expected to be significant in snow-dominated watersheds (Barnett et al. 2005; Brown and Mote 2009; Cooper et al. 2016; Sen et al. 2011). The major impact of a warmer climate will be a shift from a snow- toward a rain-dominated hydrological regime (Berghuijs et al. 2014). Many snow-dependent regions of the Northern Hemisphere are anticipated to face increasing stress from low snow years and witness changes in earlier streamflow peaks (Diffenbaugh et al. 2013; Maurer et al. 2007; Zampieri et al. 2015). Besides, several researchers have assessed potential changes in sediment loading regime at the basin level across different parts of the world (e.g., Rodríguez-Blanco et al. 2016; Shrestha et al. 2022; Siqueira et al. 2021; Zuo et al. 2016). The results illustrate a strong correlation between surface runoff and soil loss, indicating that climate change will have a noticeable impact on sediment load. Sedimentation is the primary issue for dams as it directly affects the determination of reservoir capacity and operation, leading to considerable reductions in usable storage volumes (Morris and Fan 1998; Tigrek and Aras 2012).

Edited by Dr. Hossein Hamidifar (ASSOCIATE EDITOR) / Prof. Jochen Aberle (CO-EDITOR-IN-CHIEF).

✉ Emrah Yalcin
emrah.yalcin@ahievran.edu.tr

[1] Department of Civil Engineering, Kirsehir Ahi Evran University, 40100 Kirsehir, Turkey

The Middle East region, which lies to the east of the Mediterranean Basin, is one of the most vulnerable zones to the climatic change conditions (Giorgi 2006; Lelieveld et al. 2012; Zittis et al. 2022). In this water-stressed region, severe droughts and a lack of water security have historically been significant factors leading to conflicts (Kibaroglu and Maden 2014; Munia et al. 2016). The Euphrates and Tigris are the two major snow-fed rivers of the Middle East, and their runoff is crucial for the riparian countries of Turkey, Syria, Iraq, and Iran, to produce hydroelectricity and supply water for irrigation and domestic use. Bozkurt and Sen (2013) conducted a study to examine the impacts of climate change in the Euphrates-Tigris Basin, using the dynamically downscaled hydro-climatic outputs of three coupled model intercomparison project phase 3 (CMIP3) global circulation models (GCMs) simulated under the greenhouse gas emission scenarios of A1FI (higher impact), A2 (mid-high impact), and B1 (lower impact). The findings reveal that the northern highlands of the basin in Turkey are projected to experience more adverse direct effects of climate change compared to the other riparian countries. Özdoğan (2011) conducted a comprehensive assessment to analyze the climate change impacts on the amount of water stored in the snowpack over the mountains of the Euphrates-Tigris Basin, using the simulations of 13 CMIP3 GCMs under the emission scenarios of A2 and B1. The results indicate significant decreases ranging from 10 to 60% in available snow water, particularly under the A2 scenario and later in the present century. Şen (2019) focused on river flow projections until the year 2050 for the upper portion of the Tigris Basin in Turkey, considering the statistically downscaled A2 emission scenario simulations of HADCM3 (Hadley centre coupled model, version 3) GCM from CMIP3. The study reports a streamflow reduction of about 30% after 2040. Despite the projected streamflow declines being more significant in the territories of Turkey, the other riparian countries are also expected to face the stress of diminishing water due to their downstream position. All the riparian countries have already been categorized as experiencing high or extremely high water stress by the World Resources Initiative (Gassert et al. 2013). If adequate adaptation strategies to changing climate conditions are not implemented, the consequences could worsen the prevailing water scarcity in vast areas of the region (Sümer 2015).

Despite the expected alterations in the future streamflow regime of the Euphrates-Tigris Basin, as indicated by these and several other studies (e.g., Kitoh et al. 2008; Nohara et al. 2006; Peker and Sorman 2021; Şensoy et al. 2023) based on GCM projections from the CMIP3 and CMIP5 databases, the situation could be worse than expected, according to the latest release of CMIP, the sixth phase (CMIP6). Although there is no discernible difference in the overall projections between the CMIP3 and CMIP5 ensembles (Knutti and Sedláček 2013; Kumar et al. 2014), several CMIP6 models indicate a greater degree of global warming compared to the previous generation of models throughout the twenty-first century (Forster et al. 2020). Moreover, CMIP6 encompasses several enhancements compared to its predecessors, CMIP3 and CMIP5. These enhancements primarily focus on quantifying the radiative forcing resulting from natural phenomena and human activities, such as greenhouse gas concentrations, representation of aerosol forcing, and modifications in land use (Eyring et al. 2016; Stouffer et al. 2017; Wyser et al. 2020). CMIP6 projections are based on alternative scenarios of future emissions and changes in land use, which are introduced through the new features of societal development called shared socio-economic pathways (SSPs) (O'Neill et al. 2016). Bağçaci et al. (2021) compared temperature and precipitation projections for Turkey using ensembles from the best-performing GCMs belonging to the CMIP5 and CMIP6 databases. Their findings indicate that the CMIP6 projections foresee a slightly warmer climate (up to 0.35 °C) than CMIP5. In spite of these changes in the climate projections, knowledge about the relationship between climate change and streamflow and suspended sediment load rates is limited for the Euphrates-Tigris Basin, affecting future decisions on water resources management. Although Yalcin (2023) conducted streamflow projections for Berkilin Creek, one of the upstream branches of the Tigris River, over the period 2025–2099 using CMIP6 multi-model ensembles to assess climate change impacts on the hydropower production of the Dipni Dam and hydroelectric power plant (HEPP) Project, and Yalcin (2024) assessed future changes in flood frequencies under CMIP6 climate projections for Bitlis Creek in the upper Tigris Basin, the lack of information on the future sediment loading regime of the Euphrates-Tigris Basin could cause irreversible problems, such as allocating insufficient or excessive dead storage volumes for reservoirs, due to the dam projects that continue to be designed without considering the impacts of changing climate.

The main objective of this study is to quantify the potential impacts of climate change on future streamflow and suspended sediment loading regimes in the most threatened highlands region of the Euphrates-Tigris River Basin. Bitlis Creek, one of the major branches of the Tigris River within the borders of Turkey, is selected as the study case (Fig. 1). The projected changes in the streamflow and suspended sediment load rates at the Baykan stream gauging station (SGS) on Bitlis Creek are evaluated on mean monthly, seasonal, and annual bases for the near-, mid-, and long-future periods of 2025–2049, 2050–2074, and 2075–2099, respectively. The framework of this assessment consists of five main stages: (1) development of a Soil and Water Assessment Tool (SWAT) model to simulate streamflow and suspended sediment load rates on a monthly basis at the Baykan

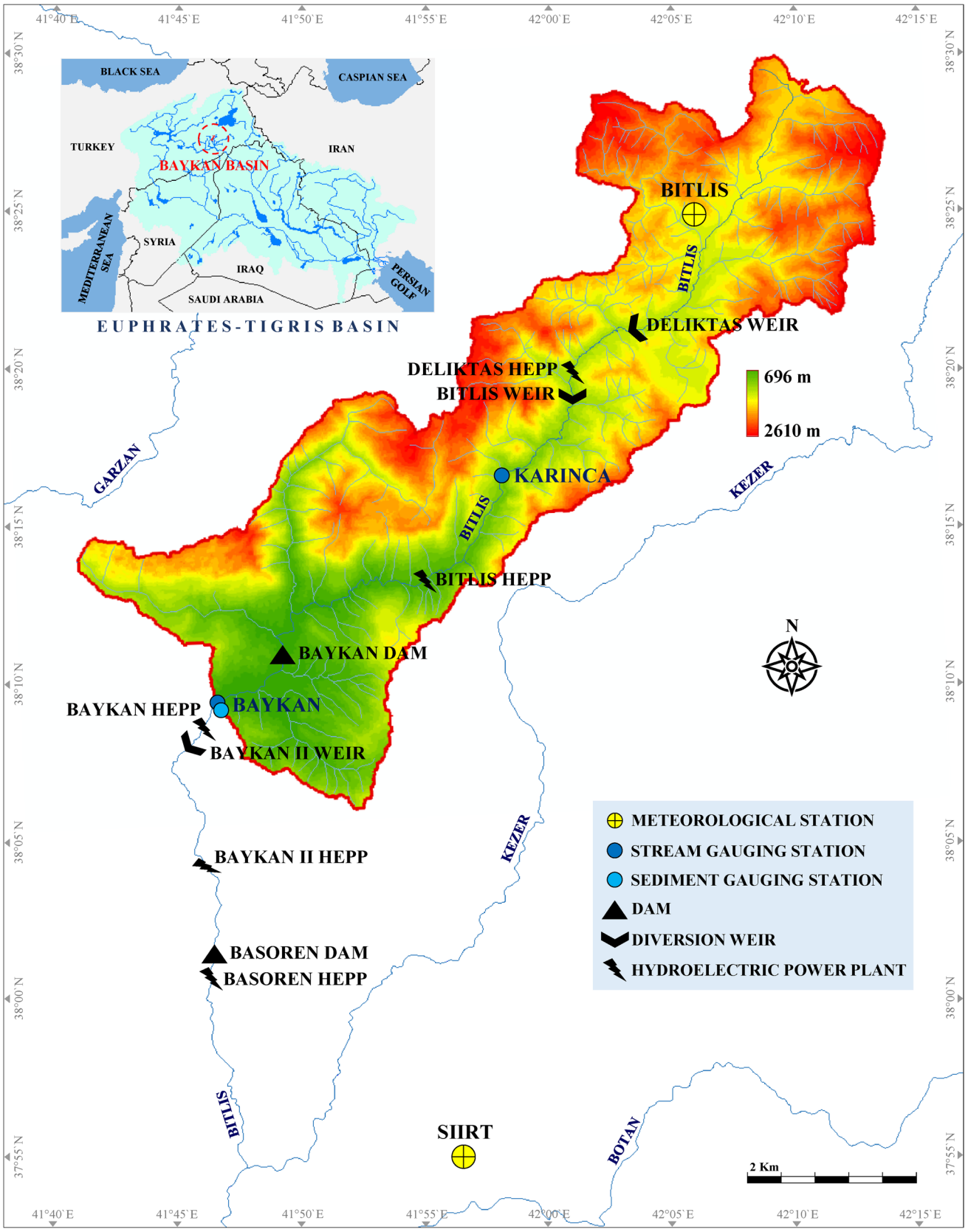

Fig. 1 Layout map of the Bitlis Creek basin along with the locations of meteorological and hydro-sedimentological stations

SGS location, (2) estimation of suspended sediment load rates for the unsampled dates of the Baykan station using the load estimator (LOADEST) software, (3) calibration and validation of the developed SWAT model using the monthly historical streamflow and suspended sediment load rates, (4) generation of multi-model ensemble-based daily maximum temperature, minimum temperature, and precipitation projections under the CMIP6 historical experiment and the medium- and high-forcing future scenarios of SSP2-4.5 and SSP5-8.5, and (5) simulation of monthly streamflow and suspended sediment load rates through the calibrated SWAT model using the historical and future climate projections. Figure 2 illustrates the flowchart of the applied methodology. The proposed methodology aims to assist in designing dam projects by considering the impacts of climate change, and the present projections are expected to provide insight into the urgent need for adaptation strategies in developing sustainable watershed management plans, not only in the Euphrates-Tigris River Basin but also in other similar basins facing the threats of climate change impacts.

Overview of the study area

The Bitlis Creek basin lies between the latitudes 37° 54' and 38° 30' N, and the longitudes 41° 36' and 42° 15' E within the borders of Bitlis and Siirt provinces in the east of Turkey, as shown in Fig. 1. Bitlis Creek originates from the southern slopes of the Southeast Taurus Mountain Range and merges with its largest branch, Kezer Creek, at an elevation of approximately 500 m before flowing into Botan Creek at about 450 m elevation. Bitlis Creek drains an area of 1076 km^2 along a 98 km flow route from its source to the conjunction with Kezer Creek. There are five cascade HEPP projects, including both storage and run-of-river (i.e., minimal storage) structures, in the planning stage with a total installed power capacity of 143 MW on the mainstream of Bitlis Creek. These projects are Deliktas Weir and HEPP, Bitlis Weir and HEPP, Baykan Dam and HEPP, Baykan II Weir and HEPP, and Basoren Dam and HEPP, respectively from upstream to downstream (Fig. 1) (DSI 2023; EIE 1990; Yolsu 2009).

The flows of Bitlis Creek are measured at two gauging stations, namely Karinca (Station ID: E26A016) and Baykan (Station ID: E26A010) (Fig. 1). The drainage areas of the Karinca and Baykan SGSs, operated by the general directorate of electrical power resources survey and development administration (EIE) until 2012 and then by the general directorate of state hydraulic works (DSI), are 346.4 and 636.5 km^2, respectively. While the Karinca station has only six years of flow records from October 1964 to September 1970, the available flow data from the Baykan station cover the period from October 1954 to September 2011 (DSI 2022a). Additionally, Baykan is the only station in the basin at which suspended sediment load measurements are conducted. Between the years 1987 and 2011, 298 sediment measurements were performed at the Baykan station (DSI 2022b). The hydro-sedimentological records of the Baykan

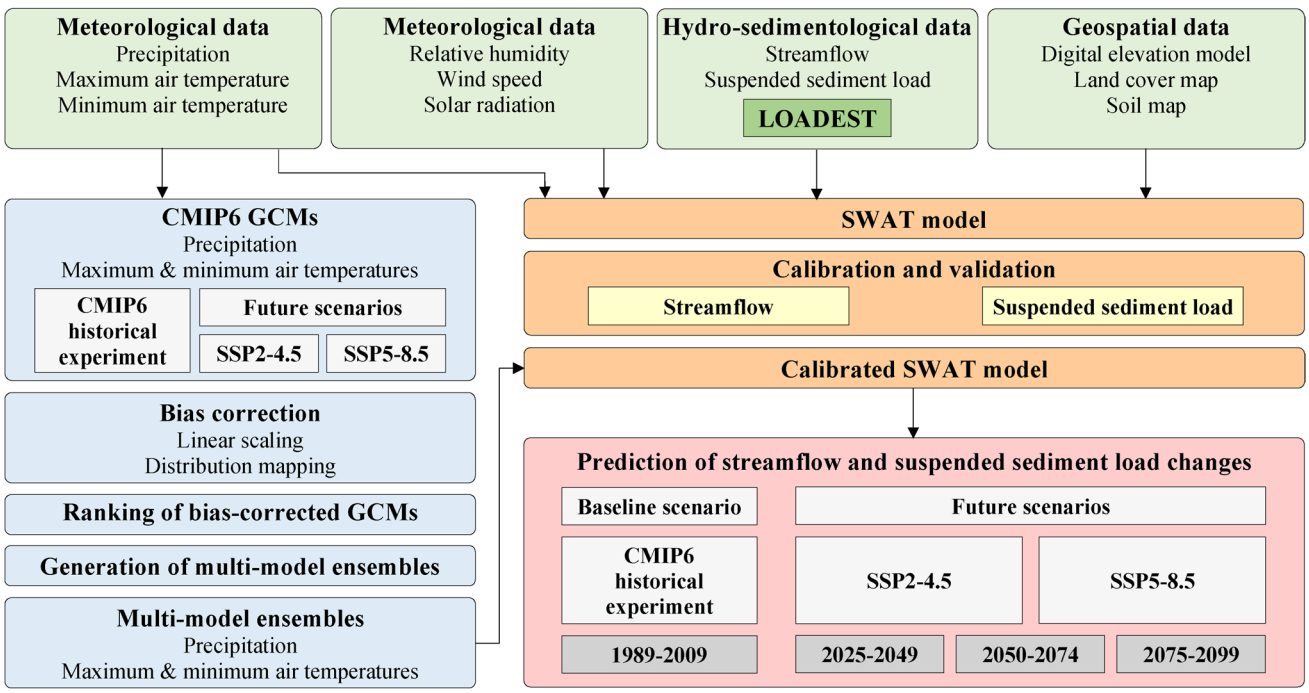

Fig. 2 Flow chart of the applied methodology

station serve as the basis for the reconnaissance and feasibility studies of the basin hydropower projects (EIE 1990; Yolsu 2009).

The climatic variables required to constitute the SWAT model of the Baykan SGS basin for streamflow and suspended sediment load simulations are precipitation, maximum and minimum temperatures, wind speed, relative humidity, and solar radiation. The Baykan basin has an average altitude of 1619 m, with maximum and minimum elevations of 2610 and 696 m, respectively. While a continental climate prevails throughout the Baykan basin, the upper portion of the catchment is in a distinctive microclimate zone characterized by excessive snowfalls resulting in snow depths up to 5 m (Aydin and Işhik 2015). In this study, the daily weather records of the Bitlis (Station ID: 17,207) and Siirt (Station ID: 17,210) meteorological stations (MSs) in the 1984–2009 period are utilized to define the climatological variability over the basin (Fig. 1) (MGM 2022b). The Bitlis and Siirt MSs are operated by the Turkish state meteorological service (MGM) at altitudes of 1573 and 895 m, respectively. Although there are other synoptic weather stations inside or near the Baykan basin (e.g., Mutki, Sarikonak, Baykan, Kayabag, and Kurtalan), the Bitlis and Siirt MSs are the only representative ones with long-term continuous weather records for all the required climatic variables.

Methodology

Modeling watershed hydrology using SWAT

SWAT is a continuous time semi-distributed hydrologic model developed by the United States Department of Agriculture—Agricultural Research Service (USDA-ARS) (Arnold et al. 2013; Neitsch et al. 2011). In this study, SWAT is preferred due to its proven success in simulating snow hydrology and future hydro-climatic changes (Peng et al. 2024; Tan et al. 2020; Troin and Caya 2014), and ArcSWAT 2012 (revision 664) is used to develop the SWAT model of the Baykan SGS basin. In the model development, the void-filled digital elevation model at 1 arc-second resolution obtained from the shuttle radar topography mission (SRTM) database (USGS 2014), land cover map at 1 km spatial resolution extracted in grid format from the global land cover 2000 (GLC2000) version 2.0 dataset (EC-JRC 2006), and grid-based soil characteristics map at a scale of 1:5 million derived from the digital soil map of the world (DSMW) version 3.6 dataset (FAO 2007) are utilized to define the physiographic conditions of the basin. The land cover, soil, and slope characteristics of the Baykan basin are presented in Fig. 3. In SWAT, the delineated watershed of the Baykan SGS is partitioned into 81 subbasins based on the provided terrain elevation data, and each of these subbasins is further divided into hydrologic response units (HRUs) having unique combinations of land cover, soil type, and topographic slope. SWAT generates a total of 586 HRUs

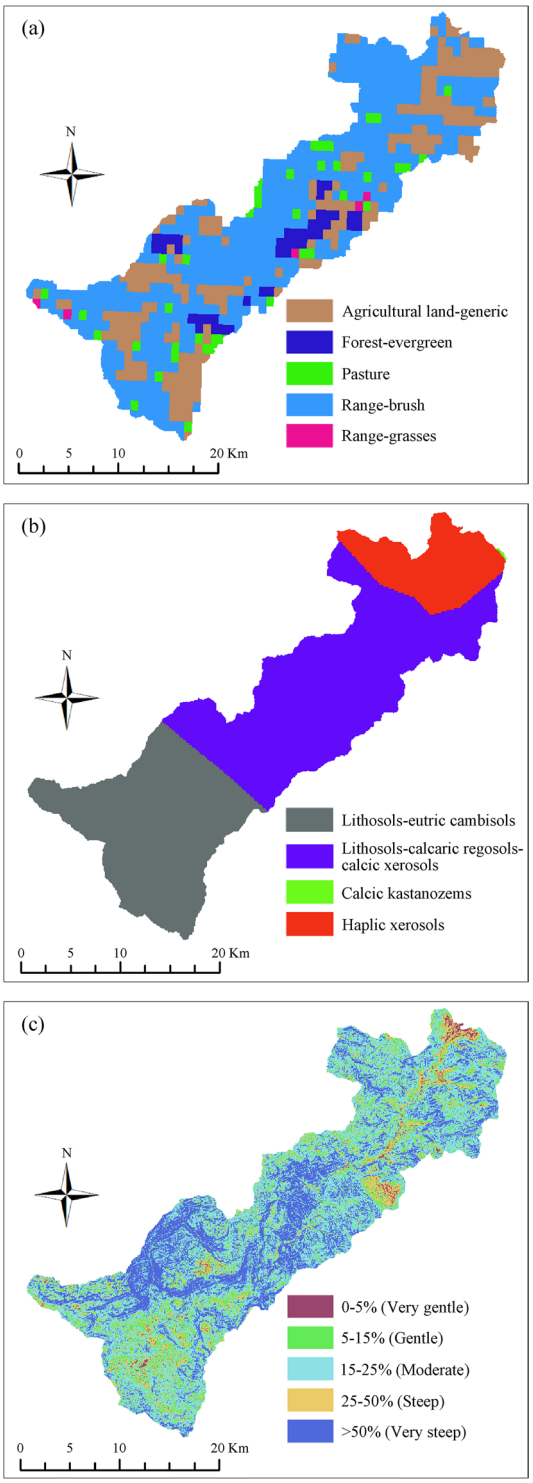

Fig. 3 Geospatial characteristics of the Bitlis SGS basin: **a** land cover, **b** soil, and **c** slope

under the given threshold percentages of 5, 5, and 15% for land cover, soil, and slope, respectively.

SWAT uses station-based weather data to simulate hydrological processes at the HRU level, which are then aggregated at the subbasin level (Neitsch et al. 2011). In order to simulate monthly runoff and suspended sediment load rates between 1989 and 2009 by providing a five-year warm-up period to mitigate the effects of initial soil–water conditions (Senent-Aparicio et al. 2020), the daily weather records of the Bitlis and Siirt MSs in the 1984–2009 period are inputted into the model together with the geographic position information and long-term mean monthly weather statistics of the stations (MGM 2022a, 2022b, 2022c). Accordingly, SWAT allocates the climate data of the Bitlis and Siirt stations, in turn, to 71 and 10 subbasins. The ratios of the total drainage areas of the subbasins represented by the Bitlis and Siirt stations to the overall catchment area are 87 and 13%, respectively. In addition, to incorporate the impacts of the mountainous terrain of the Baykan watershed on both precipitation and temperature in simulating snowpack and snowmelt processes, five elevation bands are established for all subbasins, except for those where the maximum relief is too small to account for orographic effects (Abbaspour 2015; Arnold et al. 2013).

Estimation of suspended sediment loads using LOADEST

The daily suspended sediment load measurements at the Baykan station, carried out only once a month between February 1987 and September 2011, are not sufficient alone to calibrate the developed SWAT model in a monthly time-step (Duru et al. 2018). The LOADEST program, developed by the United States geological survey (USGS), is utilized to produce a complete time series of suspended sediment loading (Runkel et al. 2004). The calibration and estimation procedures within LOADEST are based on three statistical methods, namely maximum likelihood estimation (MLE), adjusted maximum likelihood estimation (AMLE), and least absolute deviation (LAD). The AMLE and MLE methods are appropriate when the calibration model residuals (i.e., errors) are normally distributed with constant variance. LAD is an alternative method when the residuals do not adhere to the normality assumption. The AMLE method is utilized when the calibration dataset contains censored data. Under the use of uncensored data, the AMLE and MLE methods produce identical calibrated model coefficients and, hence, model fit results. The term "censored" refers to reporting a measurement as a definite value unless it falls below a specified threshold, in which case it is recorded as a non-detect at the level of that threshold (Cohn et al. 1992). In LOADEST, the primary load estimation method is AMLE. LOADEST uses suspended sediment load concentrations and corresponding streamflow data to automatically select the best regression model from the set of nine different predefined models specifying the form of the regression equation (Runkel et al. 2004). The selection is based on the statistics of the Akaike information criterion (AIC) and the Schwarz posterior probability criterion (SPPC) that are attained for the AMLE (or MLE for the use of uncensored data) results (Judge et al. 1988).

In this study, all 298 uncensored suspended sediment records, having a mean grain distribution consisting of 47.7% clay and silt and 52.3% sand, are utilized in conjunction with the observed streamflow data to calibrate the regression model with the lowest AIC and SPPC statistics (DSI 2022b). The ratio of the sum of estimated loads to the sum of observed loads (PLR) (Stenback et al. 2011) and nash–sutcliffe efficiency (NSE) (Nash and Sutcliffe 1970) statistics are utilized to diagnose bias in the load estimates. The validity of the normality assumption is checked by analyzing the linearity of the normal probability plot for the model residuals of the calibrated AMLE regression model. The linearity is also verified in terms of the probability plot correlation coefficient (PPCC) (Helsel and Hirsch 1992; Vogel 1986). In addition, the model residuals are plotted with the load estimates to examine the independence and homoscedasticity (i.e., having constant variance) of the model residuals. After verifying the two assumptions of the model fit, the daily suspended sediment load estimates of the regression model corresponding to the streamflow records for the unsampled dates within the 1989–2009 period are obtained to be used in the calibration process of the developed SWAT model (DSI 2022a).

SWAT model calibration and validation

The developed SWAT model is calibrated and validated against the monthly mean streamflow records (DSI 2022a) and the monthly total suspended sediment load estimates of LOADEST at the Baykan SGS location for the 1989–2009 period. The runoff and suspended sediment data of the initial 13-year period, from 1989 to 2001, are used for the model calibration, and the calibrated model is validated against the remaining eight years of data, from 2002 to 2009. The SWAT Calibration and Uncertainty Procedures (SWAT-CUP) software package (Abbaspour 2015) is used to perform parametrization, calibration, validation, and uncertainty analyses of the developed SWAT model. Out of the five different optimization techniques available in the SWAT-CUP package (SUFI-2, GLUE, ParaSol, McMc, and PSO), the Sequential Uncertainty Fitting version 2 (SUFI-2) algorithm (Abbaspour et al. 2004, 2007) is preferred due to the relatively fewer required number of runs to achieve acceptable calibration results (Teshager et al. 2016; Yang et al. 2008). Within the SUFI-2 algorithm, all uncertainties arising from

input datasets, conceptual model, and modeling parameters are distributed over the ranges of sensitive parameters in an iterative process. The simulation uncertainties generated by the propagation of parameter ranges using Latin hypercube sampling are quantified by the 95% prediction uncertainty, or 95PPU, in terms of the statistics of *P*-factor and *R*-factor. While the *P*-factor represents the proportion of observed data falling within the 95PPU, the *R*-factor is the ratio of the average thickness of the 95PPU band to the standard deviation of observed data (Abbaspour et al. 2015).

In this study, the calibration process of the SWAT model consists of two main stages, adjusting the flow parameters first, followed by adjusting the parameters that affect only suspended sediment load (Abbaspour 2015). Throughout the calibration process, the sensitivity of each parameter is scrutinized individually by conducting a one-at-a-time analysis with a single iteration composed of 50 simulations. Following these, a combined iteration with 500 simulations is executed with the sensitive parameters under the initial parameter ranges identified in the one-at-a-time analyses. The combined iterations are repeated by adjusting these initial ranges until acceptable *P*-factor and *R*-factor values are attained. To calibrate the model for streamflow simulations, a three-step calibration procedure is performed to mitigate problems related to parameter interaction and identifiability. The bR^2 function, defined as the coefficient of determination (R^2) multiplied by the slope of the zero-intercept linear regression line between measured and simulated variables (b), is used as the objective function of the optimization algorithm for the streamflow calibration process. The first step involves calibrating the precipitation lapse rate (PLAPS) and temperature lapse rate (TLAPS) parameters and subsequently fixing them to their best simulation values (i.e., the parameter values for the simulation with the highest bR^2 value in the last combined iteration of this step). In the second step, the same procedure is employed to calibrate the sensitive parameters related to snow. In the last step of the streamflow calibration, the other sensitive modeling parameters that pertain to groundwater (.gw), soil (.sol), management (.mgt), and main channel (.rte) input files of the model are calibrated while the location-specific parameters are held at their pre-fixed values. After adjusting the best ranges for the modeling parameters for streamflow simulations, the model calibration for both streamflow and suspended sediment load is performed by including the sensitive sediment parameters into the parameter set of the third step of the streamflow calibration. At this last stage of the calibration process, the type of the objective function is changed to the *sum* function, which is equal to the weighted summation form of the square error for the streamflow and suspended sediment load variables (Abbaspour et al. 1999).

The final iteration of the last stage of the calibration process yields the best parameter ranges, and the best simulation with the minimum objective function value of the final iteration has the best-performing parameter set of the calibration period. The best parameter ranges and best-performing parameter set attained for the calibration period are verified against the streamflow and suspended sediment data in the 2002–2009 period by performing a single combined iteration composed of 500 simulations and a single simulation, respectively. The simulation outputs of the validation period produced under the use of the best-performing parameter set of the calibration are referred to as the best simulation estimates. The model performances in simulating runoff and suspended sediment load rates in terms of the best simulation and best simulation estimates are evaluated using the monthly time series graphics and several statistical metrics, including bR^2, NSE, percent bias (PBIAS), and the ratio of the root mean square error to the standard deviation of observed data (RSR).

Performance evaluation of CMIP6 GCMs and development of multi-model ensemble predictions

In this study, the performances of 24 GCMs from the CMIP6 database are evaluated in terms of their simulations of precipitation, maximum temperature, and minimum temperature under the CMIP6 historical experiment, against the weather records of the Bitlis and Siirt stations (MGM 2022b). The daily simulations of these GCMs for the considered climate variables under the CMIP historical experiment and future scenarios of SSP2-4.5 and SSP5-8.5 are obtained from the earth system grid federation (ESGF) website (ESGF 2022). To provide consistency and comparability, only the GCMs that have daily outputs under the first ensemble member with a variant label of r1i1p1f1 are considered in the model selection. Additionally, to facilitate fair comparisons, the model datasets with different grid sizes are uniformly interpolated to a common spatial resolution of $0.5° \times 0.5°$ for the border coordinates of Turkey. This interpolation is performed using the first-order conservative remapping method (Jones 1999) within the climate data operators (CDO) software (Schulzweida 2021). The details of the selected GCMs are provided in Table 1. Before starting the evaluation process, the raw GCM data at the coordinates of the Bitlis and Siirt MSs are adjusted for possible systematic errors using two statistical bias correction methods, namely linear scaling and distribution mapping. These methods are preferred due to their proven success in the studied region (Yalcin 2023). The bias corrections are performed using the Climate Model Data for Hydrologic Modelling (CMhyd) tool (Rathjens et al. 2016).

In the first step of the evaluation process, the performances of the bias-corrected historical simulations of each GCM are analyzed on a monthly basis in terms of the modified index of agreement (*md*) (Legates and McCabe 1999),

Table 1 List of the CMIP6 GCMs used in this study

Model ID	Country	Institution	Resolution in arc degrees	
			Latitude	Longitude
ACCESS-CM2	Australia	Commonwealth Scientific and Industrial Research Organization (CSIRO) Australian Research Council Centre of Excellence for Climate System Science (ARCCSS)	1.25	1.875
ACCESS-ESM1-5	Australia	Commonwealth Scientific and Industrial Research Organization (CSIRO)	1.25	1.875
BCC-CSM2-MR	China	Beijing Climate Center (BCC)	1.112–1.121	1.125
CanESM5	Canada	Canadian Centre for Climate Modelling and Analysis (CCCma)	2.767–2.791	2.8125
CMCC-ESM2	Italy	Centro Euro-Mediterraneo sui Cambiamenti Climatici (CMCC)	0.9424084	1.25
EC-Earth3	Europe	EC-Earth Consortium	0.696–0.702	0.703125
EC-Earth3-CC	Europe	EC-Earth Consortium	0.696–0.702	0.703125
EC-Earth3-Veg	Europe	EC-Earth Consortium	0.696–0.702	0.703125
EC-Earth3-Veg-LR	Europe	EC-Earth Consortium	1.112–1.121	1.125
FGOALS-g3	China	Chinese Academy of Sciences (CAS)	2.025–5.181	2
GFDL-CM4	USA	National Oceanic and Atmospheric Administration—Geophysical Fluid Dynamics Laboratory (NOAA-GFDL)	1	1.25
GFDL-ESM4	USA	National Oceanic and Atmospheric Administration—Geophysical Fluid Dynamics Laboratory (NOAA-GFDL)	1	1.25
INM-CM4-8	Russia	Institute for Numerical Mathematics (INM)	1.5	2
INM-CM5-0	Russia	Institute for Numerical Mathematics (INM)	1.5	2
IPSL-CM6A-LR	France	Institut Pierre Simon Laplace (IPSL)	1.267606	2.5
KIOST-ESM	Korea	Korea Institute of Ocean Science and Technology (KIOST)	1.875*(precipitation data)* 1.894737*(temperature data)*	1.875
MIROC6	Japan	Japan Agency for Marine-Earth Science and Technology (JAMSTEC) Atmosphere and Ocean Research Institute—The University of Tokyo (AORI) National Institute for Environmental Studies (NIES) RIKEN Center for Computational Science (R-CCS)	1.389–1.401	1.40625
MPI-ESM1-2-HR	Germany	Max Planck Institute for Meteorology (MPI-M) Deutsches Klimarechenzentrum (DKRZ)	0.927–0.935	0.9375
MPI-ESM1-2-LR	Germany	Max Planck Institute for Meteorology (MPI-M)	1.850–1.865	1.875
MRI-ESM2-0	Japan	Meteorological Research Institute (MRI)	1.112–1.121	1.125
NESM3	China	Nanjing University of Information Science and Technology (NUIST)	1.850–1.865	1.875
NorESM2-LM	Norway	NorESM Climate Modeling Consortium	1.894737	2.5
NorESM2-MM	Norway	NorESM Climate Modeling Consortium	0.9424084	1.25
TaiESM1	Taiwan	Research Center for Environmental Changes—Academia Sinica (ASRCEC)	0.9424084	1.25

normalized root mean square error (nRMSE) (Almeida et al. 2015), Kling-Gupta efficiency metric (KGE) (Gupta et al. 2009), and fractions skill score (FSS) (Roberts and Lean 2008) statistics. In the second step, the basin-wide performance statistics are calculated by summing the products of the computed station-based performance statistics and the basin coverage ratios of the corresponding stations (i.e., 87 and 13% for the Bitlis and Siirt MSs, respectively). Based on the calculated basin-wide performance statistics, the GCMs are ranked from best to worst in terms of each performance measure for each climate variable separately. In the last step, the comprehensive rating metrics (RMs) (Chen et al. 2011) are computed for each climate variable to combine the ranks of the GCMs attained by considering the four performance measures. Accordingly, the RM-based basin-wide rankings of the GCMs for the precipitation variable are directly used in the selection of the best-performing GCMs for precipitation predictions. In the case of temperature predictions, an overall GCM ranking is derived by combining the RM-based basin-wide rankings of the GCMs for the maximum and minimum temperature variables.

After identifying the GCM rankings for precipitation and temperature predictions under the use of each bias correction method, the top-four ranked GCMs for each climate

variable are considered as the multi-model ensemble members (Ahmadalipour et al. 2017; Ahmed et al. 2019; Bağçaci et al. 2021). The daily time series of the multi-model ensembles are produced by averaging the daily bias-corrected simulations of the member GCMs for each station location. By comparing the basin-wide performance statistics of the multi-model ensemble means attained under the use of linear scaling and distribution mapping, the best-performing bias correction method, and thus the best-performing multi-model ensemble, are determined for each climate variable individually. The precipitation, maximum temperature, and minimum temperature simulations of the best-performing multi-model ensembles under the CMIP6 historical experiment for the coordinates of the Bitlis and Siirt MSs between the years 1984 and 2009, including a five-year warm-up period, are utilized as the baseline historical climate data to simulate the runoff and suspended sediment load rates in the 1989–2009 period. The best-performing multi-model ensemble means under the medium- and high-forcing scenarios of SSP2-4.5 and SSP5-8.5 in the 2020–2099 period are used to assess the potential impacts of climate change on streamflow and suspended sediment load in the Baykan SGS basin over the 2025–2099 period.

Estimating streamflow and suspended sediment load responses to climate change

The calibrated SWAT model runs are performed by introducing the precipitation and temperature predictions attained for the CMIP6 historical experiment and future scenarios of SSP2-4.5 and SSP5-8.5 at the coordinates of the Bingol and Siirt MSs. The simulated monthly runoff and suspended sediment load rates under the climate conditions of the CMIP6 historical experiment for the Baykan SGS location in the 1989–2009 period are compared with the streamflow records of the Baykan station (DSI 2022a) and the suspended sediment load estimates of LOADEST on mean monthly, seasonal, and annual bases to evaluate their appropriateness to be used as the baseline scenario in analyzing the future responses to changing climate. The climate change impacts on streamflow and suspended sediment load in the Baykan basin are assessed over 25-year time-slices for the near-, mid-, and long-future periods of 2025–2049, 2050–2074, and 2075–2099, respectively. The potential impacts of the projected changes in sediment loading on the design of water resources projects in the Baykan basin are demonstrated by analyzing the dead storage volume allocation of the Baykan Dam, planned at a 37 m higher altitude than the Baykan SGS location (EIE 1990). The mean annual totals of the suspended sediment load simulations of the SWAT model at the Baykan Dam location obtained under the climate conditions of the CMIP6 historical experiment and future scenarios of SSP2-4.5 and SSP5-8.5 are utilized to compute the total amounts of sediment accumulation in the dam reservoir under the assumption that the bed load is 25% of the suspended sediment load by considering 50- and 75-year operational lifetimes for the Baykan Dam and HEPP Project (Yalcin and Tigrek 2019). In this investigation, a horizontal deposition of sediments is assumed across the reservoir storage, and the volume-elevation curve of the reservoir (Fig. 4) (EIE 1990) is utilized to determine the reaching levels of the projected sediment accumulations.

Results and discussions

Projected changes in climate

The basin-wide performance statistics of the 24 CMIP6 GCMs in terms of their bias-corrected monthly precipitation, maximum temperature, and minimum temperature outputs under the CMIP6 historical experiment are presented in Tables 2 and 3 for the cases of using linear scaling and distribution mapping, respectively. The best simulation performance is indicated by the highest value closest to 1 for the *md*, KGE, FSS, and RM metrics and the lowest value closest to 0 for the nRMSE statistic. For the precipitation variable, the GCMs are ranked according to the descending order of their comprehensive RM values, which are calculated by considering the ranks attained by the GCMs in terms of the *md*, nRMSE, KGE, and FSS statistics. The GCM rankings for the temperature variables are based on the overall RM values computed using the individual comprehensive RM rankings of the GCMs obtained for the maximum and minimum temperature simulations. According to the acquired rankings highlighted in bold text in Tables 2 and 3, the top-four models for the precipitation and temperature variables are selected as the members of the multi-model ensembles.

The use of a small ensemble of better-performing 3 to 10 GCMs, instead of the use of the single best-performing

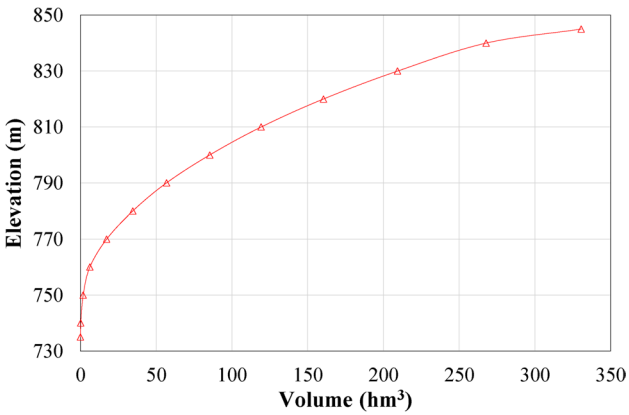

Fig. 4 Volume-elevation curve of the Baykan Dam reservoir

Table 2 Performance evaluation and ranking of the GCMs after bias correction using the linear scaling method (Bold numbers within brackets represent the ranks of GCMs)

GCM	Precipitation					Maximum temperature					Minimum temperature					Temperature
	md	nRMSE	KGE	FSS	RM (rank)	*md*	nRMSE	KGE	FSS	RM	*md*	nRMSE	KGE	FSS	RM	RM (rank)
ACCESS-CM2	0.607	0.157	0.525	0.772	0.719 **(6)**	0.880	0.080	0.960	0.988	0.125	0.856	0.081	0.925	0.957	0.271	0.167 **(21)**
ACCESS-ESM1-5	0.594	0.158	0.510	0.769	0.531 **(12)**	0.888	0.072	0.968	0.990	0.438	0.866	0.071	0.953	0.966	0.792	0.604 **(9)**
BCC-CSM2-MR	0.612	0.151	0.542	0.788	0.927 **(1)**	0.887	0.074	0.966	0.990	0.323	0.850	0.080	0.940	0.957	0.333	0.333 **(17)**
CanESM5	0.563	0.185	0.425	0.711	0.042 **(23)**	0.885	0.075	0.958	0.989	0.219	0.844	0.089	0.907	0.948	0.021	0.104 **(22)**
CMCC-ESM2	0.612	0.158	0.530	0.778	0.792 **(4)**	0.896	0.068	0.971	0.991	0.781	0.856	0.081	0.939	0.957	0.323	0.521 **(13)**
EC-Earth3	0.588	0.168	0.496	0.754	0.344 **(17)**	0.885	0.076	0.961	0.989	0.208	0.853	0.080	0.936	0.958	0.333	0.229 **(19)**
EC-Earth3-CC	0.592	0.162	0.514	0.766	0.479 **(13)**	0.888	0.074	0.957	0.990	0.292	0.861	0.075	0.916	0.963	0.385	0.354 **(15)**
EC-Earth3-Veg	0.583	0.169	0.482	0.749	0.240 **(18)**	0.884	0.075	0.964	0.989	0.229	0.856	0.077	0.940	0.961	0.458	0.354 **(16)**
EC-Earth3-Veg-LR	0.590	0.172	0.458	0.736	0.188 **(20)**	0.872	0.085	0.945	0.986	0.042	0.846	0.086	0.917	0.952	0.083	0.063 **(24)**
FGOALS-g3	0.604	0.154	0.517	0.778	0.760 **(5)**	0.892	0.069	0.970	0.991	0.677	0.861	0.074	0.948	0.964	0.615	0.667 **(7)**
GFDL-CM4	0.611	0.152	0.522	0.785	0.854 **(3)**	0.902	0.064	0.971	0.992	0.917	0.864	0.074	0.933	0.963	0.500	0.729 **(4)**
GFDL-ESM4	0.602	0.158	0.502	0.771	0.573 **(10)**	0.896	0.067	0.971	0.992	0.865	0.867	0.074	0.943	0.964	0.688	0.833 **(2)**
INM-CM4-8	0.594	0.166	0.484	0.748	0.354 **(15)**	0.892	0.070	0.970	0.991	0.615	0.871	0.071	0.943	0.967	0.802	0.729 **(5)**
INM-CM5-0	0.613	0.161	0.518	0.766	0.656 **(9)**	0.894	0.067	0.972	0.991	0.854	0.872	0.070	0.951	0.968	0.896	0.896 **(1)**
IPSL-CM6A-LR	0.615	0.154	0.547	0.784	0.906 **(2)**	0.892	0.071	0.967	0.990	0.510	0.853	0.085	0.901	0.953	0.135	0.313 **(18)**
KIOST-ESM	0.600	0.156	0.520	0.776	0.719 **(7)**	0.858	0.093	0.940	0.983	0.000	0.850	0.080	0.916	0.957	0.188	0.083 **(23)**
MIROC6	0.599	0.158	0.507	0.772	0.573 **(11)**	0.880	0.080	0.958	0.988	0.115	0.875	0.069	0.953	0.969	0.948	0.521 **(14)**
MPI-ESM1-2-HR	0.584	0.172	0.477	0.742	0.198 **(19)**	0.892	0.068	0.971	0.991	0.781	0.854	0.078	0.939	0.960	0.385	0.563 **(11)**
MPI-ESM1-2-LR	0.567	0.180	0.444	0.721	0.083 **(22)**	0.891	0.070	0.969	0.991	0.531	0.867	0.070	0.955	0.968	0.875	0.708 **(6)**
MRI-ESM2-0	0.608	0.157	0.508	0.774	0.688 **(8)**	0.892	0.071	0.965	0.990	0.469	0.865	0.073	0.926	0.965	0.594	0.542 **(12)**
NESM3	0.557	0.193	0.383	0.686	0.000 **(24)**	0.892	0.070	0.970	0.991	0.594	0.858	0.075	0.949	0.964	0.573	0.583 **(10)**
NorESM2-LM	0.587	0.163	0.494	0.761	0.365 **(14)**	0.894	0.067	0.970	0.992	0.823	0.867	0.071	0.934	0.966	0.667	0.771 **(3)**
NorESM2-MM	0.583	0.171	0.452	0.737	0.156 **(21)**	0.897	0.068	0.967	0.991	0.750	0.867	0.074	0.924	0.964	0.573	0.625 **(8)**
TaiESM1	0.592	0.167	0.485	0.753	0.354 **(16)**	0.888	0.072	0.961	0.990	0.344	0.849	0.085	0.893	0.953	0.063	0.208 **(20)**

Table 3 Performance evaluation and ranking of the GCMs after bias correction using the distribution mapping method (Bold numbers within brackets represent the ranks of GCMs)

GCM	Precipitation					Maximum temperature					Minimum temperature					Temperature
	md	nRMSE	KGE	FSS	RM (rank)	*md*	nRMSE	KGE	FSS	RM	*md*	nRMSE	KGE	FSS	RM	RM (rank)
ACCESS-CM2	0.589	0.165	0.491	0.749	0.906 **(2)**	0.887	0.076	0.964	0.989	0.031	0.859	0.077	0.933	0.961	0.063	0.021 **(24)**
ACCESS-ESM1-5	0.570	0.172	0.463	0.734	0.563 **(10)**	0.889	0.072	0.968	0.990	0.208	0.862	0.075	0.948	0.963	0.198	0.188 **(20)**
BCC-CSM2-MR	0.586	0.166	0.494	0.751	0.885 **(3)**	0.899	0.066	0.973	0.992	0.906	0.869	0.069	0.955	0.968	0.833	0.896 **(1)**
CanESM5	0.567	0.178	0.430	0.716	0.135 **(23)**	0.891	0.071	0.964	0.991	0.208	0.868	0.074	0.941	0.964	0.375	0.229 **(19)**
CMCC-ESM2	0.587	0.169	0.489	0.748	0.844 **(4)**	0.898	0.067	0.972	0.992	0.802	0.866	0.073	0.950	0.965	0.490	0.688 **(5)**
EC-Earth3	0.577	0.174	0.467	0.734	0.656 **(7)**	0.894	0.070	0.968	0.991	0.479	0.868	0.071	0.950	0.966	0.583	0.542 **(9)**
EC-Earth3-CC	0.572	0.173	0.469	0.736	0.635 **(8)**	0.894	0.070	0.964	0.991	0.354	0.868	0.070	0.931	0.967	0.531	0.479 **(13)**
EC-Earth3-Veg	0.571	0.175	0.450	0.728	0.417 **(13)**	0.890	0.071	0.968	0.991	0.250	0.866	0.071	0.949	0.967	0.552	0.438 **(15)**
EC-Earth3-Veg-LR	0.570	0.183	0.411	0.704	0.052 **(24)**	0.888	0.074	0.962	0.990	0.042	0.864	0.074	0.941	0.964	0.281	0.146 **(21)**
FGOALS-g3	0.564	0.178	0.431	0.717	0.188 **(20)**	0.895	0.067	0.972	0.991	0.750	0.863	0.072	0.951	0.965	0.479	0.646 **(7)**
GFDL-CM4	0.579	0.173	0.454	0.733	0.635 **(9)**	0.897	0.067	0.966	0.992	0.688	0.877	0.066	0.950	0.971	0.875	0.833 **(3)**
GFDL-ESM4	0.572	0.175	0.450	0.728	0.417 **(14)**	0.892	0.070	0.966	0.991	0.313	0.877	0.067	0.955	0.970	0.906	0.646 **(8)**
INM-CM4-8	0.575	0.173	0.442	0.723	0.479 **(12)**	0.892	0.069	0.970	0.991	0.542	0.867	0.073	0.937	0.964	0.375	0.396 **(17)**
INM-CM5-0	0.583	0.184	0.431	0.713	0.250 **(18)**	0.891	0.069	0.971	0.991	0.552	0.866	0.073	0.945	0.965	0.396	0.479 **(14)**
IPSL-CM6A-LR	0.596	0.165	0.508	0.757	0.948 **(1)**	0.891	0.071	0.968	0.991	0.271	0.873	0.069	0.937	0.968	0.667	0.500 **(12)**
KIOST-ESM	0.573	0.171	0.465	0.737	0.677 **(5)**	0.888	0.074	0.965	0.990	0.104	0.862	0.074	0.932	0.963	0.198	0.125 **(22)**
MIROC6	0.573	0.174	0.454	0.730	0.510 **(11)**	0.896	0.069	0.969	0.991	0.552	0.873	0.069	0.952	0.968	0.802	0.667 **(6)**
MPI-ESM1-2-HR	0.585	0.173	0.461	0.732	0.677 **(6)**	0.896	0.066	0.973	0.992	0.885	0.871	0.069	0.951	0.969	0.823	0.854 **(2)**
MPI-ESM1-2-LR	0.574	0.178	0.434	0.717	0.271 **(17)**	0.895	0.068	0.971	0.991	0.667	0.869	0.070	0.955	0.968	0.781	0.729 **(4)**
MRI-ESM2-0	0.578	0.178	0.437	0.721	0.385 **(16)**	0.896	0.069	0.967	0.991	0.573	0.868	0.071	0.928	0.966	0.469	0.542 **(10)**
NESM3	0.574	0.177	0.410	0.706	0.229 **(19)**	0.893	0.070	0.970	0.991	0.510	0.863	0.073	0.951	0.965	0.469	0.438 **(16)**
NorESM2-LM	0.556	0.180	0.436	0.719	0.167 **(22)**	0.899	0.064	0.973	0.992	0.927	0.863	0.074	0.929	0.963	0.156	0.521 **(11)**
NorESM2-MM	0.571	0.177	0.422	0.716	0.177 **(21)**	0.897	0.068	0.967	0.991	0.646	0.864	0.074	0.921	0.963	0.167	0.396 **(18)**
TaiESM1	0.572	0.175	0.448	0.726	0.396 **(15)**	0.891	0.070	0.964	0.991	0.240	0.861	0.075	0.915	0.963	0.031	0.104 **(23)**

one, is a common way to deal with large uncertainties in climate projections arising from GCM structure, assumptions, approximations, initial conditions, and parametrization (Hussain et al. 2018; Khan et al. 2018; Kim et al. 2016; Seker and Gumus 2022; Xuan et al. 2017). The basin-wide performance statistics of the multi-model ensembles are provided in Table 4. The results show that the multi-model ensembles have higher simulation performances than each of the GCMs in terms of all the considered performance measures. To determine the best-performing multi-model ensemble for each climate variable, the regionally dependent skills of the linear scaling and distribution mapping methods are evaluated by comparing the calculated performance metrics of the multi-model ensemble means (Chen et al. 2013). As detailed in Table 4, although there are no substantial differences among the corresponding metrics, the best-performing bias correction method is determined to be linear scaling for the precipitation variable and distribution mapping for the minimum and maximum temperature variables.

The statistical performances of the multi-model ensemble precipitation simulations are not satisfactory as those for the temperature simulations, especially in terms of the *md* and KGE measures. This is also the case in other studies (e.g., Ahmed et al. 2019; Bağçaci et al. 2021; Seker and Gumus 2022) that utilize different bias correction and averaging methods in producing multi-model ensemble means. Nonetheless, the monthly, seasonal, and annual averages of both precipitation and temperature simulations of the best-performing multi-model ensembles under the CMIP6 historical experiment are closely consistent with the weather records of the Bitlis and Siirt stations. The mean annual total rainfall amounts recorded in the Bitlis and Siirt MSs in the historical analysis period of 1989–2009 are 1186.43 and 676.88 mm, respectively. The mean annual total precipitation predictions of the multi-model ensemble, consisting of BCC-CSM2-MR, IPSL-CM6A-LR, GFDL-CM4, and CMCC-ESM2, for the coordinates of the Bitlis and Siirt MSs are determined, in turn, to be 1202.15 and 713.50 mm. Regarding the temperature variables, while the mean annual maximum/minimum temperature rates measured at the Bitlis and Siirt stations in the 1989–2009 period are 16.06/4.55 and 21.92/11.48 °C, the annual averages from the multi-model ensemble of BCC-CSM2-MR, MPI-ESM1-2-HR, GFDL-CM4, and MPI-ESM1-2-LR for the same period are 16.09/4.88 and 22.23/11.43 °C, respectively.

The climate projections of the multi-model ensembles under the future scenarios of SSP2-4.5 and SSP5-8.5 are evaluated on seasonal and annual bases over three future time periods, near-future (2025–2049), mid-future (2050–2074), and long-future (2075–2099), with reference

Table 4 Performance metrics comparison of the multi-model ensemble means for the identification of best-performing bias correction method. Bold statistics represent the best performance

Climate variable	Bias correction method	Member GCMs	*md*	nRMSE	KGE	FSS
Precipitation	Linear scaling	BCC-CSM2-MR IPSL-CM6A-LR GFDL-CM4 CMCC-ESM2	**0.658**	**0.126**	0.588	**0.845**
	Distribution mapping	IPSL-CM6A-LR ACCESS-CM2 BCC-CSM2-MR CMCC-ESM2	0.655	0.127	**0.597**	0.837
Maximum temperature	Linear scaling	INM-CM5-0 GFDL-ESM4 NorESM2-LM GFDL-CM4	**0.918**	0.053	0.981	0.994
	Distribution mapping	BCC-CSM2-MR MPI-ESM1-2-HR GFDL-CM4 MPI-ESM1-2-LR	**0.918**	**0.052**	**0.982**	**0.995**
Minimum temperature	Linear scaling	INM-CM5-0 GFDL-ESM4 NorESM2-LM GFDL-CM4	**0.897**	0.056	0.963	0.979
	Distribution mapping	BCC-CSM2-MR MPI-ESM1-2-HR GFDL-CM4 MPI-ESM1-2-LR	**0.897**	**0.054**	**0.969**	**0.981**

to the baseline predictions attained under the CMIP6 historical experiment. The details are presented in Table 5. Accordingly, under the SSP2-4.5 scenario, the highest decreases in mean annual total precipitation at the Bitlis and Siirt MS locations are observed in the mid-future period, with rates of 5.7 and 7.0%, respectively. All seasonal mean total precipitation decreases are below 10%, except for the declines of 11.4 and 12.2% in the winter seasons of the mid-future period and the declines of 18.7 and 18.3% in the summer seasons of the long-future period, respectively, for the Bitlis and Siirt stations. The gradual increases in mean annual maximum/minimum temperature rates at the Bitlis and Siirt station locations reach 3.17/2.49 and 3.16/2.29 °C in the long-future period, respectively. Changes in the climate are more pronounced under the SSP5-8.5 scenario compared to the SSP2-4.5. Under the SSP5-8.5 scenario, mean annual total precipitation amounts gradually decrease by 3.2, 6.1 and 15.2% for the Bitlis station and 3.9, 7.5, and 17.6% for the Siirt station in the near-, mid-, and long-future periods, respectively. While the mean total precipitation amounts of the winter and summer seasons in the mid-future period decline by 10.6 and 12.6% for the Bitlis station, respectively, the decline percentages for these seasons are determined, in turn, to be 11.6 and 10.6% for the Siirt station. The highest seasonal precipitation decreases are detected in the long-future period, with rates of 7.7 and 7.7% for the autumn months, 17.5 and 19.2% for

Table 5 Seasonal and annual comparisons of the precipitation and maximum and minimum temperature predictions for the locations of the Bitlis and Siirt MSs under the CMIP6 historical experiment and future scenarios of SSP2-4.5 and SSP5-8.5

Climate data		CMIP6 historical experiment	SSP2-4.5			SSP5-8.5		
Analysis period		1989–2009	2025–2049	2050–2074	2075–2099	2025–2049	2050–2074	2075–2099
Bitlis MS								
Mean total precipitation(mm)	Autumn	253.95	255.64	248.09	235.22	239.90	248.61	234.44
	Winter	501.86	485.08	444.45	462.94	486.84	448.81	413.80
	Spring	416.90	430.89	414.55	422.92	409.65	405.26	349.40
	Summer	29.43	27.11	26.65	23.94	27.41	25.72	21.72
	Annual	1202.15	1198.72	1133.72	1145.01	1163.80	1128.40	1019.36
Mean maximum temperature(°C)	Autumn	18.68	20.54	21.19	21.87	20.63	22.66	24.58
	Winter	2.78	4.06	4.98	6.06	4.41	6.14	7.79
	Spring	13.31	14.69	15.54	16.06	14.87	16.75	18.54
	Summer	29.39	31.24	32.14	32.85	31.18	33.24	35.36
	Annual	16.09	17.69	18.52	19.27	17.83	19.75	21.63
Mean minimum temperature(°C)	Autumn	6.18	7.44	7.88	8.24	7.57	9.12	10.57
	Winter	− 4.85	− 3.64	− 3.00	− 2.12	− 3.22	− 1.99	− 0.84
	Spring	3.36	4.27	4.72	5.09	4.36	5.64	6.84
	Summer	14.65	16.46	17.26	18.07	16.52	18.88	21.30
	Annual	4.88	6.18	6.76	7.36	6.35	7.96	9.51
Siirt MS								
Mean total precipitation (mm)	Autumn	132.46	133.87	127.63	122.85	124.45	132.08	122.25
	Winter	297.38	286.11	261.22	274.01	289.14	262.84	240.26
	Spring	273.25	277.58	265.12	267.72	262.57	255.57	217.68
	Summer	10.41	9.58	9.73	8.50	9.80	9.30	7.96
	Annual	713.50	707.13	663.71	673.08	685.96	659.79	588.15
Mean maximum temperature (°C)	Autumn	24.30	26.07	26.68	27.35	26.18	28.10	29.94
	Winter	8.62	10.08	11.19	12.34	10.55	12.48	14.26
	Spring	19.84	21.15	21.99	22.54	21.33	23.27	25.13
	Summer	35.93	37.61	38.42	39.12	37.58	39.49	41.46
	Annual	22.23	23.79	24.63	25.39	23.97	25.89	27.76
Mean minimum temperature (°C)	Autumn	12.81	14.22	14.71	15.11	14.33	16.03	17.59
	Winter	1.00	1.98	2.47	3.19	2.34	3.35	4.32
	Spring	9.36	10.29	10.76	11.16	10.35	11.75	13.17
	Summer	22.37	23.85	24.54	25.22	23.88	25.81	27.90
	Annual	11.43	12.63	13.17	13.72	12.77	14.28	15.80

the winter months, 16.2 and 20.3% for the spring months, and 26.2 and 23.5% for the summer months at the Bitlis and Siirt MS locations, respectively. Regarding temperature anomalies, the projected gradual increases in mean annual maximum/minimum temperature rates at the coordinates of the Bitlis and Siirt MSs reach 5.53/4.64 and 5.52/4.37 °C in the long-future period, respectively.

The climate projections attained under the multi-model ensemble approach are closely consistent with the climate projections of Yalcin (2024) for the Baykan SGS watershed, based on the ensemble medians of the bias-corrected daily climate simulations of 21 CMIP6 GCMs. The areal-averaged mean annual total precipitation amounts for the Baykan SGS watershed over the periods 2025–2049, 2050–2074, and 2075–2099 are projected to be 1134.92, 1072.72, and 1083.76 mm under the SSP2-4.5 scenario, and 1101.78, 1067.58, and 963.39 mm under the SSP5-8.5 scenario, respectively. In Yalcin (2024), the mean annual values of the ensemble median precipitation time series for the same periods were determined to be 1117.55, 1110.71, and 1109.32 mm under the SSP2-4.5 scenario, and 1133.38, 1113.55, and 1012.70 mm under the SSP5-8.5 scenario. Regarding temperature projections, the areal-averaged mean annual maximum/minimum temperature rates for the periods 2025–2049, 2050–2074, and 2075–2099 are projected to be 18.48/7.02, 19.31/7.59, and 20.06/8.19 °C under the SSP2-4.5 scenario, and 18.63/7.18, 20.55/8.78, and 22.42/10.33 °C under the SSP5-8.5 scenario, respectively. Although a different downscaling method (i.e., linear scaling) was utilized for the temperature simulations in Yalcin (2024), the mean annual values of the ensemble median maximum/minimum temperature time series for the same periods were observed to be 18.90/7.55, 19.87/8.40, and 20.70/9.24 °C under the SSP2-4.5 scenario, and 19.15/7.67, 21.19/9.48, and 23.86/11.56 °C under the SSP5-8.5 scenario, respectively. This high level of consistency for both precipitation and temperature variables, achieved using different ensembling approaches, increases the reliability of the future climate projections.

Suspended sediment load estimates of LOADEST

The calibration results of the best regression model of AMLE having the lowest AIC and SPPC statistics are presented as scatter plots in Fig. 5a and b. The estimated suspended sediment loads of LOADEST represent the recorded amounts at the Baykan station, with values of 1.11 and 0.88 for the PLR and NSE measures, respectively. In general, while an NSE value of 1 indicates a perfect fit, PLR values less than 1 indicate negative load bias (i.e., underestimation), and PLR values greater than 1 indicate positive load bias (i.e., overestimation). The calculated PLR and NSE values denote that the calibrated regression model can be used for load estimation after checking the model residuals for normality and constant variance assumptions. The linearity of the normal probability plot shown in Fig. 5c reveals that the model residuals follow a normal distribution. This linearity is supported by the attained value of 0.97 for the PPCC statistic, for which a value equal to 1 indicates an absolute linear relationship (Helsel and Hirsch 1992). When the model residuals are plotted with the estimated values of log load, as shown in Fig. 5d, to check their independence and homoscedasticity, it is observed that the positive and negative residuals are scattered without any clear pattern or trends. Once the model fit assumptions are confirmed for the calibration dataset, the daily suspended sediment load estimates are produced for the unsampled dates within the 1989–2009 period, as presented in Fig. 5e. The monthly totals of these estimates are utilized as "observed" data in calibrating and validating the developed SWAT model.

SWAT model performance

The calibration process of the developed SWAT model starts by fitting and then fixing two lapse rate and six snow-related parameters in two sequential steps to their best-performing values. After these modifications, the parameter ranges of ten sensitive modeling parameters related to soil, groundwater, management, and main channel are initially adjusted against the monthly streamflow records of the Baykan SGS in the 1989–2001 period by repeating combined iterations two times. To calibrate the model for suspended sediment load, three sensitive sediment-related basin (.bsn) parameters are added to the streamflow calibration parameter set, and combined iterations are repeated until acceptable simulation performances are achieved in terms of both streamflow and suspended sediment load. The parameters involved in the calibration process are listed, starting from the most sensitive one for each step, in Table 6, along with their calibrated parameter ranges and best-performing values.

The observed and simulated monthly streamflow and suspended sediment load rates at the Baykan SGS location for the calibration period are compared in Figs. 6a and 7a, respectively. In the last combined iteration performed under the calibrated parameter ranges, while a *P*-factor value of 0.88 and an *R*-factor value of 1.06 are achieved for the 95PPU band of the streamflow simulations, these factor values are observed, in turn, to be 0.97 and 1.07 for the 95PPU band of the suspended sediment load simulations. For streamflow calibration, a minimum *P*-factor value of 0.7 and an *R*-factor value of less than 1.5 (around 1) are recommended to establish the balance between the two factors (Abbaspour et al. 2015). A smaller *P*-factor with a higher *R*-factor can also be adequate for sediment load calibration (Abbaspour 2015). Based on these recommendations, the attained *P*-factor and *R*-factor values suggest

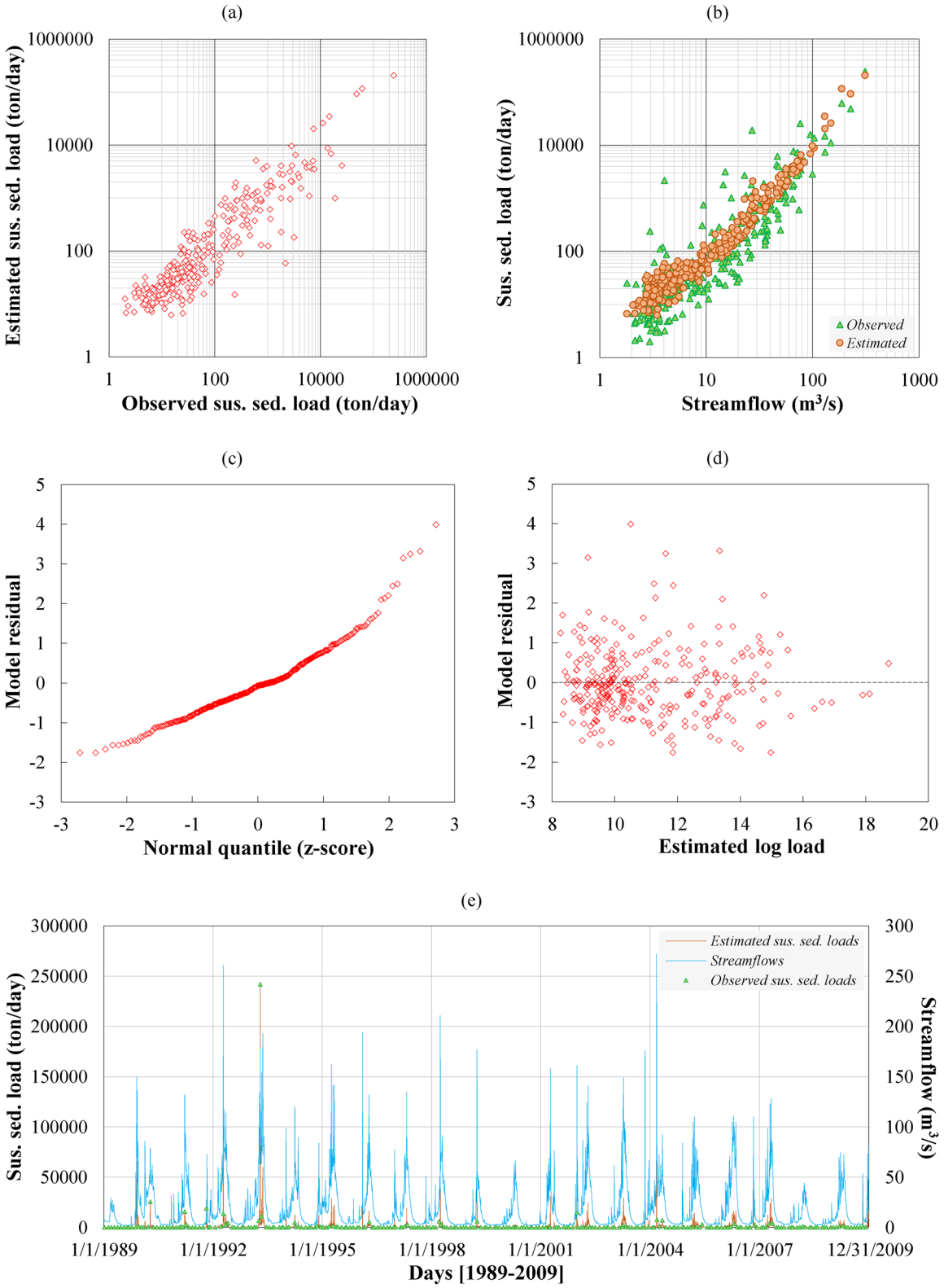

Fig. 5 LOADEST outputs: **a** comparison of the observed and estimated suspended sediment loads, **b** calibrated regression model estimates with observations from the calibration dataset, **c** normal probability plot for the model residuals, **d** estimates of log load versus model residuals, and **e** daily suspended sediment load estimates for the 1989–2009 period

Table 6 List of calibrated parameters

Sensitive parameter[a]	Calibrated parameter range	Best-performing parameter value
Calibration of precipitation and temperature lapse rates and fixing them to their best simulation values		
- Temperature lapse rate (°C/km), v__TLAPS.sub	−7.045[b]	
- Precipitation lapse rate (mm H_2O/km), v__PLAPS.sub	9.26	
Calibration of sensitive snow-related parameters and fixing them to their best simulation values		
- Snow melt base temperature (°C), v__SMTMP.bsn	1.232	
- Melt factor for snow on June 21 (mm H_2O/°C-day), v__SMFMX.bsn	6.596	
- Snowfall temperature (°C), v__SFTMP.bsn	1.566	
- Snow pack temperature lag factor, v__TIMP.bsn	0.244	
- Melt factor for snow on December 21 (mm H_2O/°C-day), v__SMFMN.bsn	8.502	
- Minimum snow water content that corresponds to 100% snow cover (mm H_2O), v__SNOCOVMX.bsn	87.119	
Calibration of other sensitive modeling parameters in the simulations of streamflow and suspended sediment load		
- Exponent parameter for calculating sediment re-entrained in channel sediment routing, v__SPEXP.bsn	[1, 1.5]	1.354
- Linear parameter for calculating the maximum amount of sediment that can be re-entrained during channel sediment routing, v__SPCON.bsn	[0.0001, 0.0002]	0.000159
- Available water capacity of the soil layer (mm H_2O/ mm soil), r__SOL_AWC().sol	[−0.84, 2.861]	−0.732
- Groundwater delay time (days), v__GW_DELAY.gw	[53.7, 351.3]	300.41
- Deep aquifer percolation fraction, v__RCHRG_DP.gw	[0.276, 0.83]	0.604
- Peak rate adjustment factor for sediment routing in the main channel, v__PRF_BSN.bsn	[0, 2]	0.926
- Initial SCS runoff curve number for moisture condition II, r__CN2.mgt	[−0.1, 0.012]	−0.041
- Threshold depth of water in the shallow aquifer required for return flow to occur (mm H_2O), v__GWQMN.gw	[1016.997, 3673.003]	1726.151
- Saturated hydraulic conductivity (mm/hr), r__SOL_K().sol	[80.708, 244.204]	88.065
- Effective hydraulic conductivity in main channel alluvium (mm/hr), v__CH_K2.rte	[240.696, 500]	246.66
- Groundwater *revap* coefficient, v__GW_REVAP.gw	[0.108, 0.2]	0.169
- Baseflow alpha factor (1/days), v__ALPHA_BF.gw	[0, 0.623]	0.115
- Depth from soil surface to bottom of layer (mm), r__SOL_Z().sol	[−0.7, 1.044]	0.257

[a] The qualifier (*v__*) refers to the substitution of a parameter by a value from the given range, while (*r__*) refers to a relative change in the parameter for which the current value is multiplied by 1 plus a factor in the given range

[b] The fixed values indicate that a parameter is fitted and then fixed

that the achieved 95PPU bands are satisfactory in terms of observed data coverage and narrowness.

Regarding the best simulation of the latest combined iteration, the bR^2, NSE, PBIAS, and RSR statistics are obtained, in turn, to be 0.92, 0.86, −9.1%, and 0.37, against the monthly streamflow measurements of the Baykan SGS, as detailed in Table 7. In the case of suspended sediment load, the best simulation statistics against the monthly totals of the daily load estimates of LOADEST are determined as 0.63, 0.77, −12.8%, and 0.48, respectively, as given in Table 8. Moriasi et al. (2007) presented a general performance rating classification for monthly streamflow and sediment load simulations based on the NSE, PBIAS, and RSR metrics. According to this classification, while monthly streamflow and sediment load simulations having an NSE value within the range of 0.75–1 and an RSR value less than 0.5 are classified as "very good", the PBIAS statistic should be less than ± 10% for streamflow and ± 15% for sediment load. For a simulation performance classified as "good", the ranges of the NSE, RSR, PBIAS (for streamflow), and PBIAS (for sediment load) statistics are 0.65–0.75, 0.5–0.6, ± 10–15%, and ± 15–30%, respectively. For a "satisfactory" simulation performance, the ranges of these statistics should be within 0.5–0.65, 0.6–0.7, ± 15–25%, and ± 30–55%, respectively. Based on this performance rating classification, the best simulation performances of the SWAT model, attained under the use of the best-performing parameter values, are categorized as very good for both streamflow and suspended sediment load. Additionally, although the *b* stat for suspended sediment load is slightly less than the targeted value of around 1, the computed R^2 statistics of 0.89 and 0.77 for the streamflow and suspended sediment load simulations,

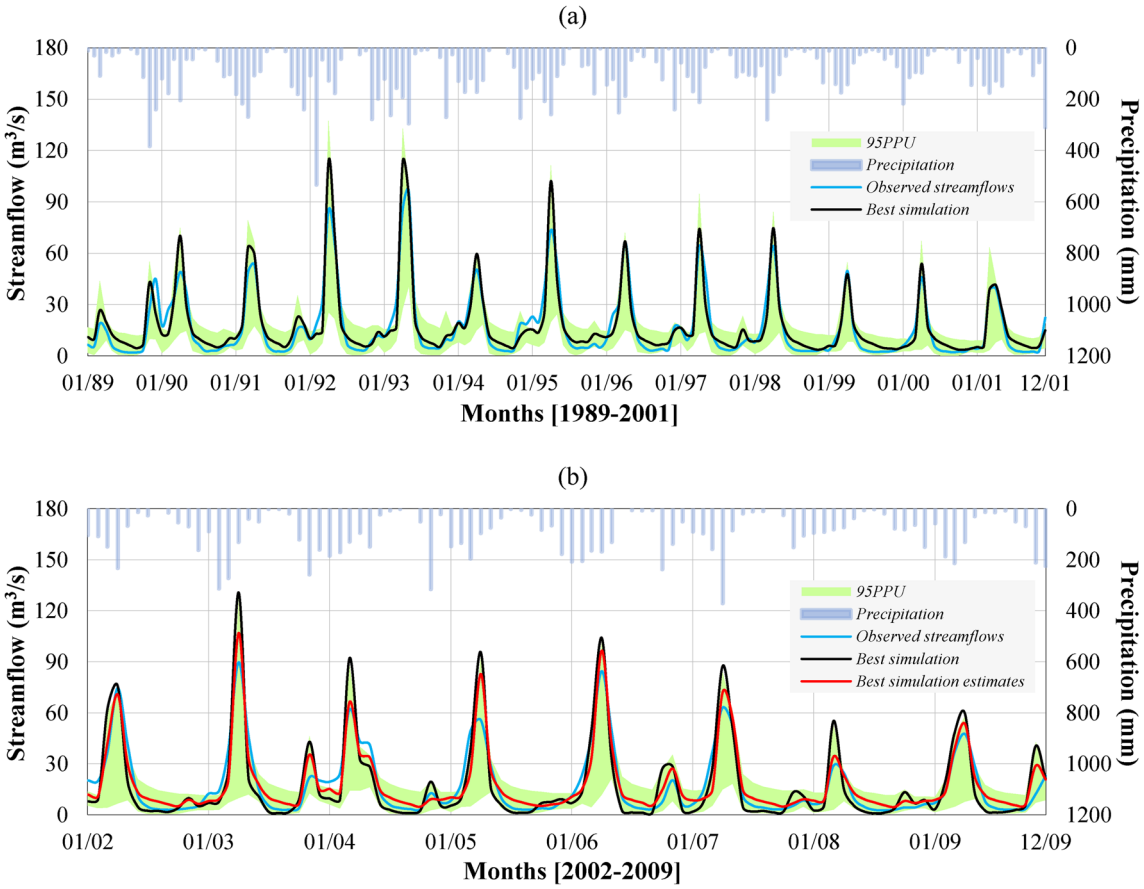

Fig. 6 Comparison of the observed and simulated monthly streamflow time series for the **a** calibration and **b** validation periods

respectively, are higher than the acceptable limit of 0.6 (Santhi et al. 2001).

The monthly time series of the streamflow and suspended sediment load simulations over the validation period from 2002 to 2009 are presented in Figs. 6b and 7b, respectively. As for the calibration period, the 95PPU bands of the streamflow and suspended sediment load simulations, produced through a single combined iteration using the calibrated parameter ranges, are reasonable in terms of the resultant *P*-factor and *R*-factor statistics. A *P*-factor value of 0.85 and an *R*-factor value of 1.09 are achieved for the 95PPU band of the streamflow simulations, while the 95PPU band for the suspended sediment load simulations has *P*-factor and *R*-factor values of 0.98 and 0.87, respectively. The statistical performance metrics of the best simulation of this combined iteration and the best simulation estimates obtained from a single run under the best-performing parameter set of the calibration are presented in Tables 7 and 8 for the streamflow and suspended sediment load simulations, respectively. Accordingly, while the performance metrics of the best simulation for suspended sediment load are similar to those determined for the calibration period, the attained values of 0.65 and 0.59 for the NSE and RSR statistics for streamflow indicate a good model performance. In the case of the best simulation estimates, the model performance in the validation period can be classified as very good for streamflow and good for suspended sediment load. The only statistic that can be deemed problematic is the *b* stat for suspended sediment load. Nevertheless, when the best simulation estimates are evaluated for the entire simulation period of 1989–2009, it is evident that the model performs reasonably well for being used in climate change analyses in terms of all the evaluation metrics (Tables 7 and 8).

Projected changes in streamflow and suspended sediment load

After verifying the monthly streamflow and suspended sediment load simulation performances of the SWAT model in terms of the best simulation estimates, the model is executed for the 1989–2009 period using the best-performing parameter set of the calibration, along with the precipitation and temperature predictions of the best-performing multi-model ensembles for the coordinates of the Bitlis and Siirt MSs under the CMIP6 historical experiment. The simulation results are then compared with the streamflow records of

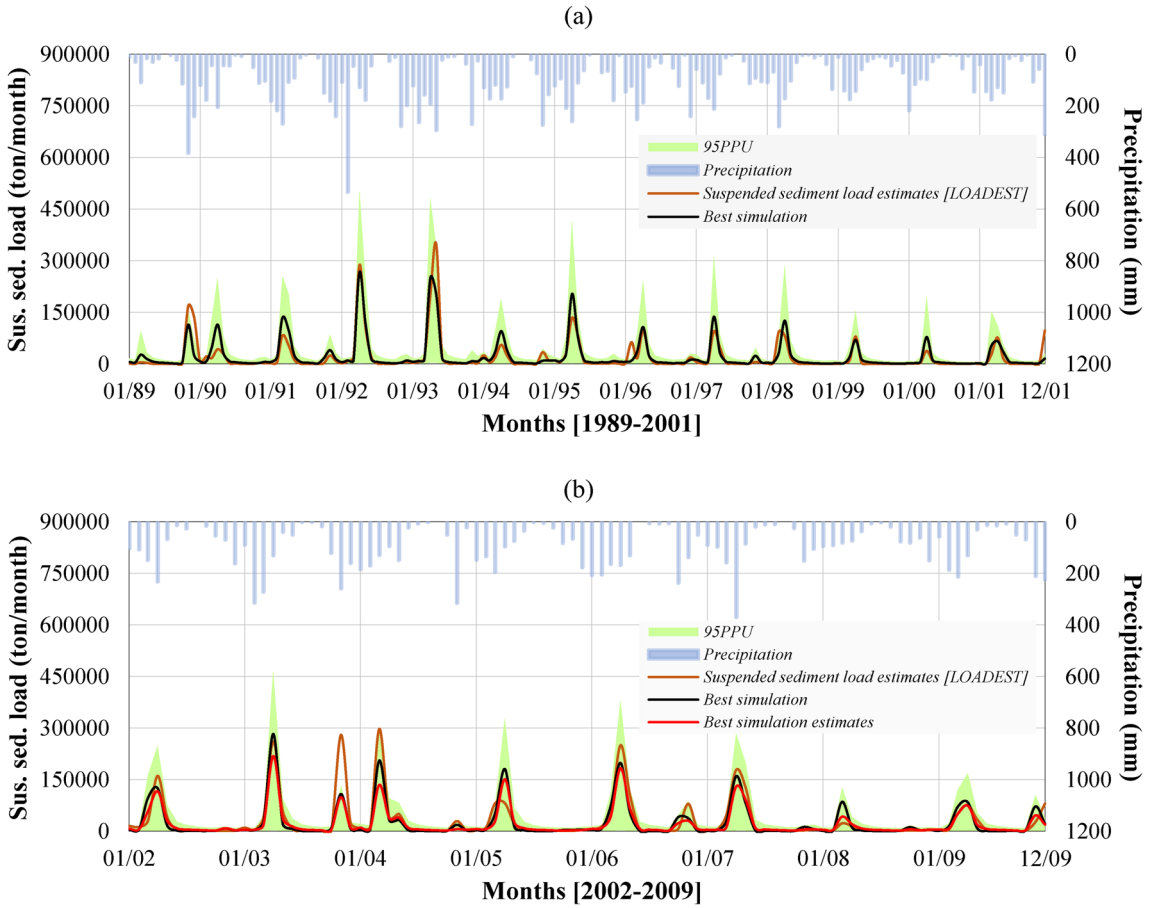

Fig. 7 Comparison of the observed and simulated monthly suspended sediment load time series for the **a** calibration and **b** validation periods

Table 7 Statistical performance indices for the streamflow simulations

Model simulation	R^2	b	NSE	PBIAS (%)	RSR	Mean (m^3/s)		Standard deviation (m^3/s)	
						Simulation	Observed	Simulation	Observed
Calibration period (1989–2001)									
Best simulation	0.89	1.03	0.86	−9.1	0.37	18.33	16.80	20.75	19.02
Validation period (2002–2009)									
Best simulation	0.81	1.18	0.65	0.5	0.59	17.83	17.93	25.50	19.56
Best simulation estimates	0.87	0.96	0.86	−5.0	0.37	18.82		20.10	
Whole simulation period (1989–2009)									
Best simulation estimates	0.88	1.00	0.86	−7.6	0.37	18.53	17.23	20.54	19.23

the Baykan SGS and the suspended sediment load estimates from LOADEST to analyze the usability of these simulations as the baseline scenario for assessing future changes in the near-, mid-, and long-future periods. Accordingly, while the mean runoff rates from the Baykan SGS are 5.50, 13.16, 43.67, 6.59, and 17.23 m^3/s during autumn, winter, spring, summer, and annually, respectively, from 1989 to 2009, the means of the simulated streamflow rates attained under the climate conditions of the CMIP6 historical experiment are determined to be 6.31, 12.45, 46.85, 10.46, and 19.02 m^3/s. In the case of suspended sediment load, while the mean suspended sediment load amounts from LOADEST are 11,205.95, 11,102.47, 70,520.05, 1887.37, and 23,678.96 tons/month during autumn, winter, spring, summer, and annually, respectively, the simulated amounts are observed to be 8727.80, 7303.25, 69,844.84, 5556.54, and 22,858.11 tons/month. Since relatively similar streamflow and suspended sediment load averages are simulated

Table 8 Statistical performance indices for the suspended sediment load simulations

Model simulation	R^2	b	NSE	PBIAS (%)	RSR	Mean (ton/month)		Standard deviation (ton/month)	
						Simulation	Observed	Simulation	Observed
Calibration period (1989–2001)									
Best simulation	0.77	0.82	0.77	− 12.8	0.48	22,671.20	20,093.73	44,423.89	47,662.35
Validation period (2002–2009)									
Best simulation	0.78	0.74	0.77	15.1	0.48	25,036.92	29,504.95	50,738.26	60,792.95
Best simulation estimates	0.81	0.59	0.74	23.8	0.51	22,475.57		40,145.86	
Whole simulation period (1989–2009)									
Best simulation estimates	0.76	0.70	0.76	4.4	0.49	22,632.40	23,678.96	42,913.35	53,245.61

using the climate predictions under the CMIP6 historical experiment, the model runs are continued for the 2025–2099 period with the precipitation and temperature projections under the SSP2-4.5 and SSP5-8.5 scenarios. Considering the simulation results obtained under the CMIP6 historical experiment as the baseline scenario, the projected streamflow and suspended sediment load changes are analyzed in three 25-year future periods of 2025–2049, 2050–2074, and 2075–2099. These changes are examined on both seasonal and annual bases, as presented in Table 9.

Under the SSP2-4.5 scenario, no notable changes are detected in the mean streamflow and suspended sediment load projections for the autumn and summer seasons. However, while a gradual increase in both the mean streamflow and suspended sediment load projections is observed for the winter months, a gradual decrease is monitored for the spring months throughout the future periods. In the near-future period, the mean streamflow rate and mean monthly suspended sediment load amount for the winter season increase by 13.8 and 23.8%, respectively. These increases further escalate to 33.7 and 62.3% in the long-future period. Conversely, the mean streamflow rate and mean monthly suspended sediment load amount for the spring months decline by 19.3 and 34.3% in the long-future period. On an annual basis, the decreases in the mean streamflow and suspended sediment load projections are 8.5 and 20.1% for the mid-future period, respectively. The decrease percentages are determined, in turn, to be 7.1 and 21.4% for the long-future period. The gradual changes in the streamflow rates and suspended sediment load amounts for the winter and spring seasons are much more pronounced under the SSP5-8.5 scenario. The increases of 11.5 and 20.2% for the winter runoff and suspended sediment load rates in the near-future period reach 39.1 and 73.5% in the long-future period, respectively. Conversely, the declines of 10.6 and 19.7% for the spring runoff and suspended sediment load rates in the near-future period reach, in turn, 40.9 and 60.0% in the long-future period. Furthermore, on an annual basis, while the mean streamflow rates in the near-, mid-, and long-future periods are 5.4, 9.1, and 20.9% less than the historical average, the reductions in the mean monthly suspended sediment load amount for these periods are determined

Table 9 Seasonal and annual comparisons of the streamflow and suspended sediment load estimates for the Baykan station location under the CMIP6 historical experiment and future scenarios of SSP2-4.5 and SSP5-8.5

Climate data		CMIP6 historical experiment	SSP2-4.5			SSP5-8.5		
Analysis period		1989–2009	2025–2049	2050–2074	2075–2099	2025–2049	2050–2074	2075–2099
Mean streamflow rate (m^3/s)	Autumn	6.31	6.51	6.05	6.27	6.21	6.59	6.17
	Winter	12.45	14.16	14.56	16.64	13.87	17.05	17.31
	Spring	46.85	44.17	39.20	37.81	41.87	35.88	27.69
	Summer	10.46	9.97	9.76	9.91	10.01	9.63	9.01
	Annual	19.02	18.70	17.39	17.66	17.99	17.28	15.04
Mean suspended sediment load (ton/month)	Autumn	8727.80	9163.98	8738.33	9021.06	8707.33	9598.53	9309.86
	Winter	7303.25	9041.63	9538.27	11,850.00	8775.33	12,432.96	12,668.05
	Spring	69,844.84	61,258.40	49,794.40	45,879.47	56,104.40	41,965.79	27,918.47
	Summer	5556.54	5125.76	4943.57	5080.45	5166.44	4836.37	4329.53
	Annual	22,858.11	21,147.44	18,253.64	17,957.75	19,688.38	17,208.41	13,556.48

to be 13.9, 24.7, and 40.7%, respectively. When comparing the projected mean annual streamflow and precipitation changes, it is evident that the streamflow reductions align with the decreases in precipitation (Tables 5 and 9). A potential increase in evapotranspiration within the basin, driven by warmer temperatures and less precipitation, may explain the slightly greater reduction percentages in streamflow compared to precipitation. Comparing the mean annual decreases in the suspended sediment load rates with the streamflow reductions, it becomes apparent that the impact of changing climate on suspended sediment loading is more pronounced than on streamflow. Peng et al. (2024) reported similar findings in their future projections of streamflow and sediment yield for the Ishikari River Basin (Japan), using climate projections from two CMIP6 GCMs under four different SSP scenarios. Their study indicated that a projected temperature increase of 3.05 °C and a 7% decrease in precipitation could lead to reductions of 7% in streamflow and 14% in sediment yield across this cold region basin.

For both future scenarios, the projected streamflow rates for the snow accumulation months of December, January, February, and March show a noticeable increase compared to the historical period. However, the projected runoffs for April and May, which correspond to the snowmelt season for the basin, demonstrate a significant decrease compared to the historical period. These changes in the spring and winter streamflow regimes do not align with the precipitation projections obtained for the same seasons (Tables 5 and 9). Hence, it can be inferred that precipitation will not fall as snow in the future winters as much as in the past due to rising temperatures. This inference was also made by Yalcin (2024) for the ensemble median streamflow projections based on daily SWAT model simulations for the Baykan station location under the climate projections of 21 CMIP6 GCMs. In addition, consistent streamflow projections were estimated by Yalcin (2024) for both future scenarios. The mean annual values of the ensemble median daily streamflow projection time series for the periods 2025–2049, 2050–2074, and 2075–2099 were determined to be 16.42, 15.79, and 16.31 m^3/s under the SSP2-4.5 scenario, and 16.33, 15.88, and 14.05 m^3/s under the SSP5-8.5 scenario, respectively. Moreover, a similar inference was presented by Yalcin (2023) for the future streamflow regime of Berkilin Creek, another upstream branch of the Tigris River, utilizing the CMIP6 multi-model ensemble projections. For both the SSP2-4.5 and SSP5-8.5 scenarios, projections for Berkilin Creek indicated an increase in streamflow during the snow accumulation months, while decreases were anticipated during the snow depletion months. Additionally, the annual streamflow reductions obtained for Bitlis Creek closely align with those observed for Berkilin Creek. Average annual streamflow decreases for Berkilin Creek were estimated to be 1.4, 6.3, and 5.7% under the SSP2-4.5 scenario, and 0.6, 7.0, and 17.6% under the SSP5-8.5 scenario, for the periods 2025–2049, 2050–2074, and 2075–2099, respectively. Furthermore, the expected inference aligns with the projections of Şensoy et al. (2023) for snow duration, snow cover extent, and snow water equivalent in the snow-dominated Karasu and Murat subbasins of the Euphrates River, which share similar climatic and topographical characteristics with the Bitlis Creek basin. Their CMIP5-based projections revealed a dramatic shrinkage of over 65% in snow cover extent, a 25% decrease in snow duration, and a noticeable reduction of over 50% in snow water equivalent for the 2075–2099 period.

The potential impacts of the projected changes in the suspended sediment loading regime of the basin on the dead storage volume requirement of the Baykan Dam are investigated based on the monthly suspended sediment load simulations of the SWAT model at the dam location, obtained under the climate conditions of the CMIP6 historical experiment and future scenarios of SSP2-4.5 and SSP5-8.5. Assuming a ratio of bed load to suspended sediment load of 25%, the total sediment volume that will accumulate in the Baykan Dam reservoir (i.e., suspended sediment load plus bed load) is analyzed separately for 50- and 75-year operational lifetimes by using the mean annual total suspended sediment load projections, as detailed in Table 10. Accordingly, for a 50-year operational lifetime, the amount of sediment expected to be deposited in the reservoir volume is computed as 13.09 hm^3 under the climate conditions of the CMIP6 historical experiment. The corresponding dead volume allocation requirements are determined to be 11.05 and 10.26 hm^3 under the SSP2-4.5 and SSP5-8.5 scenarios, respectively. For a 75-year operational lifetime, the required dead volume allocations are calculated to be 19.64, 16.01, and 13.90 hm^3 for the climate conditions of the CMIP6 historical experiment, SSP2-4.5, and SSP5-8.5 scenarios, respectively. The results indicate that a dead storage allocation based on the historical climate conditions may lead to an active storage capacity loss of up to 2.83 or 5.74 hm^3, due to the positioning of the intake structure at an elevation up to 2.55 or 4.41 m higher, depending on the considered operational lifetime of 50 or 75 years, respectively. The Baykan Dam and HEPP Project, planned based on the hydro-sedimentological records of the Baykan station, has not yet commenced construction. Therefore, considering the projected changes in the streamflow and suspended sediment loading regimes, it is necessary to reconsider the project planning and design in light of future climatic conditions to achieve the targeted return in the coming decades. The projected gradual increases in the winter runoffs and decreases in the spring runoffs through the future periods highlight the need to re-optimize the installed power capacity of the project and, accordingly, reconfigure the hydropower production components, such as turbines, penstocks, and energy

Table 10 Comparison of the total sediment load accumulation estimates for the Baykan Dam reservoir over the 50- and 75-year operational lifetime periods under the CMIP6 historical experiment and future scenarios of SSP2-4.5 and SSP5-8.5

Operational lifetime		50-year			75-year		
Climate data		CMIP6 historical experiment	SSP2-4.5	SSP5-8.5	CMIP6 historical experiment	SSP2-4.5	SSP5-8.5
Simulation data period		1989–2009	2025–2074	2025–2074	1989–2009	2025–2099	2025–2099
Mean streamflow rate	m^3/s	17.78	16.91	16.53	17.78	16.79	15.74
Mean suspended sediment load	ton/year	276,469.81	233,284.60	216,760.72	276,469.81	225,438.99	195,668.32
	m^3/year	209,446.83	176,730.76	164,212.67	209,446.83	170,787.11	148,233.58
Mean bed load	ton/year	69,117.45	58,321.15	54,190.18	69,117.45	56,359.75	48,917.08
	m^3/year	52,361.71	44,182.69	41,053.17	52,361.71	42,696.78	37,058.39
Mean total sediment load	ton/year	345,587.26	291,605.75	270,950.90	345,587.26	281,798.73	244,585.40
	m^3/year	261,808.53	220,913.45	205,265.83	261,808.53	213,483.89	185,291.97
Total sediment volume	hm^3	13.09	11.05	10.26	19.64	16.01	13.90
Minimum water level	m	766.22	764.37	763.67	771.36	768.85	766.95

tunnels. Potential decreases in the hydropower production capacity of the Baykan HEPP due to the projected declines in the streamflow rates for the coming decades can be partially mitigated by increasing the active storage capacity of the reservoir through repositioning of the intake structure.

Conclusions

This study assesses how the changing climate alters streamflow and suspended sediment loading regimes in the most threatened highlands region of the Euphrates-Tigris Basin, with a focus on Bitlis Creek. The hydro-sedimentological measurements from the Baykan station on Bitlis Creek are projected through the SWAT model simulations on a monthly time-step, utilizing the precipitation and temperature predictions of the best-performing multi-model ensembles under the CMIP6 historical experiment and the medium- and high-forcing future scenarios of SSP2-4.5 and SSP5-8.5. The high consistency between the simulated streamflow and suspended sediment load rates under the climate conditions of the CMIP6 historical experiment and the historical measurements of the Baykan station indicates the success of the applied methodology in this study. Furthermore, the concurrence of the streamflow projections with the ensemble median streamflow projections of Yalcin (2024), based on daily SWAT model simulations for the Baykan station location under the climate projections of 21 CMIP6 GCMs, supports the robustness of the applied methodology. Additionally, the agreement between the projected changes for the streamflow regime of Bitlis Creek and those obtained by Yalcin (2023) for Berkilin Creek, which exhibits similar climate and topographic characteristics to Bitlis Creek, enhances the reliability of the future projections attained within the scope of the study. The outcomes of this assessment can be summarized as follows:

- The gradual increases in the mean annual maximum/minimum temperature rates over the watershed of the Baykan station reach up to 3.16/2.29 °C and 5.52/4.37 °C in the long-future period under the SSP2-4.5 and SSP5-8.5 scenarios, respectively.
- While the mean annual total precipitation amount over the Baykan basin experiences the highest reduction, with a rate of 7.0%, in the mid-future period under the SSP2-4.5 scenario, the precipitation decreases become more substantial under the SSP5-8.5 scenario, reaching 7.5% in the mid-future period and 17.6% in the long-future period.
- The projected changes in climate lead to 8.5 and 9.1% decreases in the mean annual streamflow rates of Bitlis Creek at the Baykan station location in the mid-future period and 7.1 and 20.9% decreases in the long-future period under the SSP2-4.5 and SSP5-8.5 scenarios, respectively.
- The mean annual suspended sediment loading rate at the Baykan station location is projected to decline at rates of 7.5, 20.1, and 21.4% under the SSP2-4.5 scenario, and 13.9, 24.7, and 40.7% under the SSP5-8.5 scenario in the near-, mid-, and long-future periods, respectively.
- The shift in the precipitation pattern from snowy winters to rainy winters results in substantial increases for the winter months and more significant decreases for the spring months compared to the annual declines in the streamflow and suspended sediment load projections.
- Under the SSP2-4.5 scenario, the long-future period is projected to experience increases of 33.7 and 62.3% in the streamflow and suspended sediment load rates during the winter season, respectively. In contrast, the spring

season is expected to witness declines of 19.3 and 34.3%, respectively. Under the SSP5-8.5 scenario, the long-future period is projected to have increases of 39.1 and 73.5% in the winter streamflow and suspended sediment load rates, while the spring season is expected to see declines of 40.9 and 60.0%, respectively.

According to the results of this study, it is observed that the warming and drying climate will significantly alter the streamflow and suspended sediment loading regimes in this high-altitude sub-catchment of the Euphrates-Tigris Basin. Therefore, it is necessary to develop appropriate strategies at the planning and management levels to mitigate the potential adverse impacts of climate change on the hydroelectricity production of the HEPP projects on Bitlis Creek. It is important to note that the findings of this research should not be generalized for the entire Euphrates-Tigris River Basin due to its complex and heterogeneous climate and topography. Consequently, it is recommended to conduct site-specific assessments using the proposed methodology for the planning and management of water resources projects within the Euphrates-Tigris Basin. The lack of recent measurements from the synoptic stations, which limits the historical analysis period of the study to 1989–2009, also prevents an evaluation of which climate scenario is more appropriate to be considered for planning and management purposes by comparing historical records with the future projections over the period from 2015 (i.e., the start of the future projections of the GCMs) to 2025 (i.e., the start of the future periods considered). In addition, since the hydro-sedimentological projections of this study are based on monthly SWAT model simulations with multi-model ensemble time series produced by averaging the daily bias-corrected simulations of the member GCMs, they cannot capture extreme rainfall events that often cause excessive erosion during periods of low vegetation cover (Shrestha and Jetten 2018; Vrieling et al. 2014). Thus, for future studies, it is advised to carry out daily assessments using higher-quality geospatial datasets in the hydrological model construction to incorporate the impacts of extreme events, especially on suspended sediment load projections. Moreover, further research experimenting with different bias correction methods and averaging approaches in producing multi-model ensemble means is recommended to increase the accuracy of precipitation predictions. The proposed methodology can be further enriched by integrating future changes in other climatic variables, such as relative humidity, solar radiation, and wind speed, in simulating streamflow and suspended sediment load projections (Gorguner and Kavvas 2020). In conclusion, it is thought that the results of this assessment will help raise awareness of the need to implement efficient adaptation measures for the sustainability of water resources projects in the Euphrates-Tigris Basin in the coming decades.

Author contributions EY: conceptualization, methodology, writing—review and editing.

Funding No funding was received to assist with the preparation of this manuscript.

Data availability Data will be made available on reasonable request.

Declarations

Conflict of interest The author declares no competing interests.

References

Abbaspour KC, Sonnleitner MA, Schulin R (1999) Uncertainty in estimation of soil hydraulic parameters by inverse modeling: example lysimeter experiments. Soil Sci Soc Am J 63(3):501–509. https://doi.org/10.2136/sssaj1999.03615995006300030012x

Abbaspour KC, Johnson CA, van Genuchten MT (2004) Estimating uncertain flow and transport parameters using a sequential uncertainty fitting procedure. Vadose Zone J 3(4):1340–1352. https://doi.org/10.2136/vzj2004.1340

Abbaspour KC, Yang J, Maximov I, Siber R, Bogner K, Mieleitner J, Zobrist J, Srinivasan R (2007) Modelling hydrology and water quality in the pre-alpine/alpine Thur watershed using SWAT. J Hydrol 333(2–4):413–430. https://doi.org/10.1016/j.jhydrol.2006.09.014

Abbaspour KC, Rouholahnejad E, Vaghefi S, Srinivasan R, Yang H, Kløve B (2015) A continental-scale hydrology and water quality model for Europe: calibration and uncertainty of a high-resolution large-scale SWAT model. J Hydrol 524:733–752. https://doi.org/10.1016/j.jhydrol.2015.03.027

Abbaspour KC (2015) SWAT-CUP2: SWAT calibration and uncertainty programs - a user manual. Eawag - Swiss Federal Institute of Aquatic Science and Technology, Duebendorf

Adam JC, Hamlet AF, Lettenmaier DP (2009) Implications of global climate change for snowmelt hydrology in the twenty-first century. Hydrol Process 23(7):962–972. https://doi.org/10.1002/hyp.7201

Ahmadalipour A, Rana A, Moradkhani H, Sharma A (2017) Multi-criteria evaluation of CMIP5 GCMs for climate change impact analysis. Theor Appl Climatol 128:71–87. https://doi.org/10.1007/s00704-015-1695-4

Ahmed K, Sachindra DA, Shahid S, Demirel MC, Chung E-S (2019) Selection of multi-model ensemble of general circulation models for the simulation of precipitation and maximum and minimum temperature based on spatial assessment metrics. Hydrol Earth Syst Sci 23(11):4803–4824. https://doi.org/10.5194/hess-23-4803-2019

Almeida MP, Perpiñán O, Narvarte L (2015) PV power forecast using a nonparametric PV model. Sol Energy 115:354–368. https://doi.org/10.1016/j.solener.2015.03.006

Arnold JG, Kiniry JR, Srinivasan R, Williams JR, Haney EB, Neitsch SL (2013) SWAT 2012 input/output documentation. Texas Water Resources Institute, Texas

Aydin MC, Işhik E (2015) Evaluation of ground snow loads in the micro-climate regions. Russ Meteorol Hydrol 40(11):741–748. https://doi.org/10.3103/S1068373915110047

Bağçaci SÇ, Yucel I, Duzenli E, Yilmaz MT (2021) Intercomparison of the expected change in the temperature and the precipitation retrieved from CMIP6 and CMIP5 climate projections: a Mediterranean hot spot case. Turkey Atmos Res 256:105576. https://doi.org/10.1016/j.atmosres.2021.105576

Barnett TP, Adam JC, Lettenmaier DP (2005) Potential impacts of a warming climate on water availability in snow-dominated regions. Nature 438:303–309. https://doi.org/10.1038/nature04141

Berghuijs WR, Woods RA, Hrachowitz M (2014) A precipitation shift from snow towards rain leads to a decrease in streamflow. Nat Clim Change 4:583–586. https://doi.org/10.1038/nclimate2246

Bozkurt D, Sen OL (2013) Climate change impacts in the Euphrates-Tigris Basin based on different model and scenario simulations. J Hydrol 480:149–161. https://doi.org/10.1016/j.jhydrol.2012.12.021

Brown RD, Mote PW (2009) The response of Northern Hemisphere snow cover to a changing climate. J Clim 22(8):2124–2145. https://doi.org/10.1175/2008JCLI2665.1

Chen W, Jiang Z, Li L (2011) Probabilistic projections of climate change over China under the SRES A1B scenario using 28 AOGCMs. J Climate 24(17):4741–4756. https://doi.org/10.1175/2011JCLI4102.1

Chen J, Brissette FP, Chaumont D, Braun M (2013) Finding appropriate bias correction methods in downscaling precipitation for hydrologic impact studies over North America. Water Resour Res 49(7):4187–4205. https://doi.org/10.1002/wrcr.20331

Cohn TA, Gilroy EJ, Baier WG (1992) Estimating fluvial transport of trace constituents using a regression model with data subject to censoring. In: Proceedings of the joint statistical meeting, Boston, August 9–13, 1992, pp 142–151

Cooper MG, Nolin AW, Safeeq M (2016) Testing the recent snow drought as an analog for climate warming sensitivity of Cascades snowpacks. Environ Res Lett 11(8):084009. https://doi.org/10.1088/1748-9326/11/8/084009

Diffenbaugh NS, Scherer M, Ashfaq M (2013) Response of snow-dependent hydrologic extremes to continued global warming. Nat Clim Change 3:379–384. https://doi.org/10.1038/nclimate1732

DSI (General Directorate of State Hydraulic Works) (2022a) Electrical power resources survey and development administration (EIE) - flow gauging yearbooks (1935–2011). General directorate of state hydraulic works, Ankara

DSI (General Directorate of State Hydraulic Works) (2022b) Suspended sediment data and sediment transport amounts for the Bitlis Creek - Baykan sediment gauging station (Station ID: E26A010). General Directorate of State Hydraulic Works, Ankara

DSI (General directorate of state hydraulic Works) (2023) Water usage agreements. https://enerji.dsi.gov.tr/Sayfa/Detay/774. Accessed 10 March 2023

Duru U, Arabi M, Wohl EE (2018) Modeling stream flow and sediment yield using the SWAT model: a case study of Ankara River basin. Turkey Phys Geogr 39(3):264–289. https://doi.org/10.1080/02723646.2017.1342199

EC-JRC (European Commission - Joint Research Centre) (2006) The global land cover 2000 (GLC2000) products. https://forobs.jrc.ec.europa.eu/products/glc2000/products.php. Accessed 28 June 2022

EIE (Electrical Power Resources Survey and Development Administration) (1990) Bitlis Creek reconnaissance report. Electrical Power Resources Survey and Development Administration, Ankara

ESGF (Earth System Grid Federation) (2022) WCRP coupled model intercomparison Project (Phase 6). https://esgf-node.llnl.gov/projects/cmip6/. Accessed 15 May 2022

Eyring V, Bony S, Meehl GA, Senior CA, Stevens B, Stouffer RJ, Taylor KE (2016) Overview of the coupled model intercomparison project phase 6 (CMIP6) experimental design and organization. Geosci Model Dev 9(5):1937–1958. https://doi.org/10.5194/gmd-9-1937-2016

FAO (food and agriculture organization of the united nations) (2007) Digital soil map of the world (DSMW). https://www.fao.org/geonetwork/srv/en/metadata.show?id=14116. Accessed 28 June 2022

Forster PM, Maycock AC, McKenna CM, Smith CJ (2020) Latest climate models confirm need for urgent mitigation. Nat Clim Change 10:7–10. https://doi.org/10.1038/s41558-019-0660-0

Gassert F, Reig P, Luo T, Maddocks A (2013) Aqueduct country and river basin rankings: a weighted aggregation of spatially distinct hydrological indicators. https://www.wri.org/data/water-stress-country. Accessed 26 April 2023

Giorgi F (2006) Climate change hot-spots. Geophys Res Lett 33(8):L08707. https://doi.org/10.1029/2006GL025734

Gorguner M, Kavvas ML (2020) Modeling impacts of future climate change on reservoir storages and irrigation water demands in a Mediterranean basin. Sci Total Environ 748:141246. https://doi.org/10.1016/j.scitotenv.2020.141246

Gupta HV, Kling H, Yilmaz KK, Martinez GF (2009) Decomposition of the mean squared error and NSE performance criteria: implications for improving hydrological modelling. J Hydrol 377(1–2):80–91. https://doi.org/10.1016/j.jhydrol.2009.08.003

Helsel DR, Hirsch RM (1992) Statistical methods in water resources. Elsevier, Amsterdam

Hussain M, Yusof KW, Mustafa MRU, Mahmood R, Jia S (2018) Evaluation of CMIP5 models for projection of future precipitation change in Bornean tropical rainforests. Theor Appl Climatol 134:423–440. https://doi.org/10.1007/s00704-017-2284-5

Immerzeel WW, Lutz AF, Andrade M, Bahl A, Biemans H, Bolch T, Hyde S, Brumby S, Davies BJ, Elmore AC, Emmer A, Feng M, Fernández A, Haritashya U, Kargel JS, Koppes M, Kraaijenbrink PDA, Kulkarni AV, Mayewski PA, Nepal S, Pacheco P, Painter TH, Pellicciotti F, Rajaram H, Rupper S, Sinisalo A, Shrestha AB, Viviroli D, Wada Y, Xiao C, Yao T, Baillie JEM (2020) Importance and vulnerability of the world's water towers. Nature 577:364–369. https://doi.org/10.1038/s41586-019-1822-y

Jones PW (1999) First- and second-order conservative remapping schemes for grids in spherical coordinates. Mon Weather Rev 127(9):2204–2210. https://doi.org/10.1175/1520-0493(1999)127%3c2204:FASOCR%3e2.0.CO;2

Judge GG, Hill RC, Griffiths WE, Lütkepohl H, Lee T-C (1988) Introduction to the theory and practice of econometrics. John Wiley and Sons, New York

Khan N, Shahid S, Ahmed K, Ismail T, Nawaz N, Son M (2018) Performance assessment of general circulation model in simulating daily precipitation and temperature using multiple gridded datasets. Water 10(12):1793. https://doi.org/10.3390/w10121793

Kibaroglu A, Maden TE (2014) An analysis of the causes of water crisis in the Euphrates-Tigris river basin. J Environ Stud Sci 4:347–353. https://doi.org/10.1007/s13412-014-0185-9

Kim J, Ivanov VY, Fatichi S (2016) Climate change and uncertainty assessment over a hydroclimatic transect of Michigan. Stoch Environ Res Risk Assess 30:923–944. https://doi.org/10.1007/s00477-015-1097-2

Kitoh A, Yatagai A, Alpert P (2008) First super-high-resolution model projection that the ancient "Fertile Crescent" will disappear in this century. Hydrol Res Lett 2:1–4. https://doi.org/10.3178/hrl.2.1

Knutti R, Sedláček J (2013) Robustness and uncertainties in the new CMIP5 climate model projections. Nat Clim Change 3:369–373. https://doi.org/10.1038/nclimate1716

Kumar D, Kodra E, Ganguly AR (2014) Regional and seasonal intercomparison of CMIP3 and CMIP5 climate model ensembles for temperature and precipitation. Clim Dyn 43:2491–2518. https://doi.org/10.1007/s00382-014-2070-3

Legates DR, McCabe GJ (1999) Evaluating the use of "goodness-of-fit" measures in hydrologic and hydroclimatic model validation. Water Resour Res 35(1):233–241. https://doi.org/10.1029/1998WR900018

Lelieveld J, Hadjinicolaou P, Kostopoulou E, Chenoweth J, El Maayar M, Giannakopoulos C, Hannides C, Lange MA, Tanarhte M, Tyrlis E, Xoplaki E (2012) Climate change and impacts in the Eastern

Mediterranean and the Middle East. Clim Change 114:667–687. https://doi.org/10.1007/s10584-012-0418-4
Maurer EP, Stewart IT, Bonfils C, Duffy PB, Cayan D (2007) Detection, attribution, and sensitivity of trends toward earlier streamflow in the Sierra Nevada. J Geophys Res 112(D11):D11118. https://doi.org/10.1029/2006JD008088
MGM (Turkish State Meteorological Service) (2022a) Annual maximum precipitation records in standard times for the Bitlis and Siirt meteorological stations (Station IDs: 17207 and 17210). Turkish State Meteorological Service, Ankara
MGM (Turkish State Meteorological Service) (2022b) Daily precipitation, maximum and minimum air temperature, wind speed, solar radiation, and relative humidity records of the Bitlis and Siirt meteorological stations (Station IDs: 17207 and 17210). Turkish State Meteorological Service, Ankara
MGM (Turkish State Meteorological Service) (2022c) Long-term all parameters bulletin for the Bitlis and Siirt meteorological station (Station IDs: 17207 and 17210). Turkish State Meteorological Service, Ankara
Milano M, Reynard E, Köplin N, Weingartner R (2015) Climatic and anthropogenic changes in Western Switzerland: impacts on water stress. Sci Total Environ 536:12–24. https://doi.org/10.1016/j.scitotenv.2015.07.049
Moriasi DN, Arnold JG, Van Liew MW, Bingner RL, Harmel RD, Veith TL (2007) Model evaluation guidelines for systematic quantification of accuracy in watershed simulations. T Asabe 50(3):885–900. https://doi.org/10.13031/2013.23153
Morris GL, Fan J (1998) Reservoir sedimentation handbook: design and management of dams, reservoirs, and watersheds for sustainable use. McGraw-Hill, New York
Munia H, Guillaume JHA, Mirumachi N, Porkka M, Wada Y, Kummu M (2016) Water stress in global transboundary river basins: significance of upstream water use on downstream stress. Environ Res Lett 11(1):014002. https://doi.org/10.1088/1748-9326/11/1/014002
Nash JE, Sutcliffe JV (1970) River flow forecasting through conceptual models part I - a discussion of principles. J Hydrol 10(3):282–290. https://doi.org/10.1016/0022-1694(70)90255-6
Neitsch SL, Arnold JG, Kiniry JR, Williams JR (2011) Soil and Water Assessment Tool theoretical documentation version 2009. Texas Water Resources Institute, Texas
Nohara D, Kitoh A, Hosaka M, Oki T (2006) Impact of climate change on river discharge projected by multimodel ensemble. J Hydrometeorol 7(5):1076–1089. https://doi.org/10.1175/JHM531.1
O'Neill BC, Tebaldi C, van Vuuren DP, Eyring V, Friedlingstein P, Hurtt G, Knutti R, Kriegler E, Lamarque J-F, Lowe J, Meehl GA, Moss R, Riahi K, Sanderson BM (2016) The scenario model intercomparison project (ScenarioMIP) for CMIP6. Geosci Model Dev 9(9):3461–3482. https://doi.org/10.5194/gmd-9-3461-2016
Özdoğan M (2011) Climate change impacts on snow water availability in the Euphrates-Tigris basin. Hydrol Earth Syst Sci 15(9):2789–2803. https://doi.org/10.5194/hess-15-2789-2011
Peker IB, Sorman AA (2021) Application of SWAT using snow data and detecting climate change impacts in the mountainous eastern regions of Turkey. Water 13(14):1982. https://doi.org/10.3390/w13141982
Peng S, Mihara K, Xu X, Kuramochi K, Toma Y, Hatano R (2024) Modeling hydrological processes under multi-model projections of climate change in a cold region of Hokkaido. Japan Catena 234:107605. https://doi.org/10.1016/j.catena.2023.107605
Rathjens H, Bieger K, Srinivasan R, Chaubey I, Arnold JG (2016) CMhyd user manual: documentation for preparing simulated climate change data for hydrologic impact studies. https://swat.tamu.edu/media/115265/bias_cor_man.pdf. Accessed 25 May 2022
Roberts NM, Lean HW (2008) Scale-selective verification of rainfall accumulations from high-resolution forecasts of convective events. Mon Weather Rev 136(1):78–97. https://doi.org/10.1175/2007MWR2123.1
Rodríguez-Blanco ML, Arias R, Taboada-Castro MM, Nunes JP, Keizer JJ, Taboada-Castro MT (2016) Potential impact of climate change on suspended sediment yield in NW Spain: a case study on the Corbeira Catchment. Water 8(10):444. https://doi.org/10.3390/w8100444
Runkel RL, Crawford CG, Cohn TA (2004) Load Estimator (LOADEST): a FORTRAN program for estimating constituent loads in streams and rivers. United States Geological Survey (USGS), Virginia
Santhi C, Arnold JG, Williams JR, Dugas WA, Srinivasan R, Hauck LM (2001) Validation of the SWAT model on a large river basin with point and nonpoint sources. J Am Water Resour as 37(5):1169–1188. https://doi.org/10.1111/j.1752-1688.2001.tb03630.x
Schulzweida U (2021) CDO user guide version 2.0.5. Max Planck Institute for Meteorology, Hamburg
Seker M, Gumus V (2022) Projection of temperature and precipitation in the Mediterranean region through multi-model ensemble from CMIP6. Atmos Res 280:106440. https://doi.org/10.1016/j.atmosres.2022.106440
Sen OL, Unal A, Bozkurt D, Kindap T (2011) Temporal changes in the Euphrates and Tigris discharges and teleconnections. Environ Res Lett 6(2):024012. https://doi.org/10.1088/1748-9326/6/2/024012
Şen Z (2019) Climate change expectations in the upper Tigris River basin, Turkey. Theor Appl Climatol 137:1569–1585. https://doi.org/10.1007/s00704-018-2694-z
Senent-Aparicio J, Alcalá FJ, Liu S, Jimeno-Sáez P (2020) Coupling SWAT model and CMB method for modeling of high-permeability bedrock basins receiving interbasin groundwater flow. Water 12(3):657. https://doi.org/10.3390/w12030657
Şensoy A, Uysal G, Doğan YO, Civelek HS (2023) The future snow potential and snowmelt runoff of Mesopotamian water tower. Sustainability 15(8):6646. https://doi.org/10.3390/su15086646
Shrestha DP, Jetten VG (2018) Modelling erosion on a daily basis, an adaptation of the MMF approach. Int J Appl Earth Obs Geoinf 64:117–131. https://doi.org/10.1016/j.jag.2017.09.003
Shrestha S, Bhatta B, Talchabhadel R, Virdis SGP (2022) Integrated assessment of the landuse change and climate change impacts on the sediment yield in the Songkhram River Basin. Thailand Catena 209:105859. https://doi.org/10.1016/j.catena.2021.105859
Siqueira PP, Oliveira PTS, Bressiani D, Neto AAM, Rodrigues DB (2021) Effects of climate and land cover changes on water availability in a Brazilian Cerrado basin. J Hydrol Reg Stud 37:100931. https://doi.org/10.1016/j.ejrh.2021.100931
Stenback GA, Crumpton WG, Schilling KE, Helmers MJ (2011) Rating curve estimation of nutrient loads in Iowa rivers. J Hydrol 396(1–2):158–169. https://doi.org/10.1016/j.jhydrol.2010.11.006
Stouffer RJ, Eyring V, Meehl GA, Bony S, Senior C, Stevens B, Taylor KE (2017) CMIP5 scientific gaps and recommendations for CMIP6. Bull Am Meteorol Soc 98(1):95–105. https://doi.org/10.1175/BAMS-D-15-00013.1
Sümer V (2015) Climate change and water issues in Mesopotamia: a framework for fostering transboundary cooperation in Euphrates-Tigris Basin. In: Filho WL (ed) Handbook of climate change adaptation. Springer, Heidelberg, pp 1685–1700
Tan ML, Gassman PW, Yang X, Haywood J (2020) A review of SWAT applications, performance and future needs for simulation of hydro-climatic extremes. Adv Water Resour 143:103662. https://doi.org/10.1016/j.advwatres.2020.103662
Teshager AD, Gassman PW, Secchi S, Schoof JT, Misgna G (2016) Modeling agricultural watersheds with the soil and water assessment tool (SWAT): calibration and validation with a novel

procedure for spatially explicit HRUs. Environ Manage 57:894–911. https://doi.org/10.1007/s00267-015-0636-4
Tigrek S, Aras T (2012) Reservoir sediment management. CRC Press, Boca Raton
Troin M, Caya D (2014) Evaluating the SWAT's snow hydrology over a Northern Quebec watershed. Hydrol Process 28(4):1858–1873. https://doi.org/10.1002/hyp.9730
USGS (United States Geological Survey) (2014) Shuttle Radar Topography Mission (SRTM): 1 arc-second global elevation database. https://earthexplorer.usgs.gov/. Accessed 28 June 2022
Viviroli D, Weingartner R, Messerli B (2003) Assessing the hydrological significance of the world's mountains. Mt Res Dev 23(1):32–40. https://doi.org/10.1659/0276-4741(2003)023[0032:ATHSOT]2.0.CO;2
Viviroli D, Dürr HH, Messerli B, Meybeck M, Weingartner R (2007) Mountains of the world, water towers for humanity: typology, mapping, and global significance. Water Resour Res 43(7):W07447. https://doi.org/10.1029/2006WR005653
Vogel RM (1986) The probability plot correlation coefficient test for the normal, lognormal, and Gumbel distributional hypotheses. Water Resour Res 22(4):587–590. https://doi.org/10.1029/WR022i004p00587
Vrieling A, Hoedjes JCB, van der Velde M (2014) Towards large-scale monitoring of soil erosion in Africa: accounting for the dynamics of rainfall erosivity. Glob Planet Change 115:33–43. https://doi.org/10.1016/j.gloplacha.2014.01.009
Wyser K, Kjellström E, Koenigk T, Martins H, Döscher R (2020) Warmer climate projections in EC-Earth3-Veg: the role of changes in the greenhouse gas concentrations from CMIP5 to CMIP6. Environ Res Lett 15(5):054020. https://doi.org/10.1088/1748-9326/ab81c2
Xuan W, Ma C, Kang L, Gu H, Pan S, Xu Y-P (2017) Evaluating historical simulations of CMIP5 GCMs for key climatic variables in Zhejiang Province, China. Theor Appl Climatol 128:207–222. https://doi.org/10.1007/s00704-015-1704-7
Yalcin E (2023) Quantifying climate change impacts on hydropower production under CMIP6 multi-model ensemble projections using SWAT model. Hydrol Sci J 68(13):1915–1936. https://doi.org/10.1080/02626667.2023.2245815
Yalcin E (2024) Assessing future changes in flood frequencies under CMIP6 climate projections using SWAT modeling: a case study of Bitlis Creek. Turkey J Water Clim Change 15(5):2212–2231. https://doi.org/10.2166/wcc.2024.646
Yalcin E, Tigrek S (2019) The Tigris hydropower system operations: the need for an integrated approach. Int J Water Resour D 35(1):110–125. https://doi.org/10.1080/07900627.2017.1369867
Yang J, Reichert P, Abbaspour KC, Xia J, Yang H (2008) Comparing uncertainty analysis techniques for a SWAT application to the Chaohe Basin in China. J Hydrol 358(1–2):1–23. https://doi.org/10.1016/j.jhydrol.2008.05.012
Yolsu (Yolsu Engineering Services Incorporated Company) (2009) Basoren HEPP feasibility report. Yolsu Engineering Services Incorporated Company, Ankara
Zampieri M, Scoccimarro E, Gualdi S, Navarra A (2015) Observed shift towards earlier spring discharge in the main Alpine rivers. Sci Total Environ 503–504:222–232. https://doi.org/10.1016/j.scitotenv.2014.06.036
Zittis G, Almazroui M, Alpert P, Ciais P, Cramer W, Dahdal Y, Fnais M, Francis D, Hadjinicolaou P, Howari F, Jrrar A, Kaskaoutis DG, Kulmala M, Lazoglou G, Mihalopoulos N, Lin X, Rudich Y, Sciare J, Stenchikov G, Xoplaki E, Lelieveld J (2022) Climate change and weather extremes in the Eastern Mediterranean and Middle East. Rev Geophys 60(3):e2021RG000762. https://doi.org/10.1029/2021RG000762
Zuo D, Xu Z, Yao W, Jin S, Xiao P, Ran D (2016) Assessing the effects of changes in land use and climate on runoff and sediment yields from a watershed in the Loess Plateau of China. Sci Total Environ 544:238–250. https://doi.org/10.1016/j.scitotenv.2015.11.060